A semi-analytical solution for shale gas production from compressible matrix including scaling of gas recovery

Pål Ø. Andersen [a,b]

[a] *Dep. of Energy Resources, University of Stavanger, 4036, Norway*
[b] *The National IOR Centre of Norway, University of Stavanger, 4036, Norway*

ABSTRACT

The aim of this work is to present semi-analytical solutions for shale gas production from a 1D porous medium, where constant pressure is assumed at one side and a no-flow boundary at the other. Adsorbed gas is modeled by a Langmuir isotherm, the gas and rock are compressible, porosity reduction reduces intrinsic permeability and apparent permeability further depends on the Knudsen number.

The partial differential equation describing this system can be formulated as a nonlinear diffusion equation in terms bulk gas density M. This system is comparable to a form described for spontaneous imbibition with semi-analytical solutions regardless of the shape of the diffusion coefficient as function of the conserved property, in that case fluid saturation. Semi-analytical solutions are thus obtained that can give spatial profiles, at given times, of pressure, adsorption, porosity and apparent permeability, in addition to time profiles of gas recovery. These solutions are valid until the no-flow boundary is encountered (the critical time). Late time behavior is investigated using numerical solutions. The roles of system length, adsorption isotherm, rock compressibility, porosity-permeability relations and non-Darcy effects are examined.

It is shown that gas recovery follows a square root of time profile before the critical time. Scaling yields full overlap of recovery curves until their critical time. The square root of time solution is valid for recoveries around 12–22%, but is a good approximation until obtainable recoveries of 35–50% for typical shale cases. Cases where the diffusion coefficient increases more steeply with M leave the square root profile at lower recovery values and obtain slower recovery with time systematically according to the steepness of the coefficient.

1. Introduction

Technical advances in drilling, well completion and well stimulation have allowed economic development of tight shale gas and accelerated its production the last two decades (Mullen, 2010). Shale gas resources are found worldwide including China, Argentina, US, Russia, Australia and more, with 7299 tcf estimated technically recoverable in 2013 (Kuuskraa et al., 2013). Gas shales are organic-rich fine-grained source rocks with nano-to microdarcy permeability (Javadpour et al., 2007; Mullen, 2010) and poor connectivity such that the generated gas was stored there geologically. The typical pore size distribution of shales is in the order of nanometer, where the majority of pores are in organic kerogen or inorganic clay-rich matrix. To produce the shale gas, multi-lateral horizontal wells are drilled and completed with multistage hydraulic fractures. The fracturing is usually performed with large volumes of water with proppant material (sand or ceramic solid particles) to keep the fractures open and able to produce over time. Production takes place

by pressure depletion. The fractures can close if they are poorly propped, the fracture closure stress/drawdown is high or the shale is geomechanically weak. Fracture conductivity and its alterations are of great influence to production (Cipolla et al., 2010; Yu and Sepehrnoori, 2014; Berawala et al., 2019).

Shale gas is stored in the matrix pores and microfractures as free gas, but also in significant amounts adsorbed to the kerogen and clays or absorbed (dissolved) in the organic material (Darishchev et al., 2013; Swami et al., 2013; Pan and Connell, 2015; Klewiah et al., 2020). This gas can be mobilized to free gas upon pressure depletion. Unlike for conventional gas reservoirs, sorbed gas can be a very important storage mechanism in shales (and coals), and has been reported to account for between 20 and 85% of the gas in place (Kuuskraa et al., 1985; Curtis, 2002; Mengal and Wattenbarger, 2011). The large adsorption is related to strong interaction between gas molecules and the surface in confined spaces which increases the storage capacity compared to the free gas that could occupy the same pore space as adsorbed gas is packed more

densely. Although much gas in place can be in sorbed form, it may contribute more significantly to production at late times since more desorption takes place the lower the pressure is. The role of desorption was described in simulation studies of US shales Barnett and Marcellus (Cipolla et al., 2010; Yu and Sepehrnoori, 2014; Pan and Connell, 2015). Enhanced shale gas desorption and recovery can take place by CO_2 huff-and-puff operations since CO_2, under many conditions, is measured to have greater adsorption affinity and capacity (up to five times higher) than methane (Nuttal et al., 2005; Heller and Zoback, 2014; Klewiah et al., 2020).

Apart from permeability being ultra-low, the permeability can be pressure dependent: When the mean free path of gas molecules becomes comparable to the characteristic pore dimension (this ratio is called the Knudsen number (Knudsen, 1909; Florence et al., 2007; Javadpour et al., 2007)) gas molecules collide more with the wall than with each other. The gas molecules can bounce, slip or diffuse on the surface in addition to the free flow in the central pores. This results in a larger 'apparent' permeability than the intrinsic permeability expected only from free flow (Darcy flow) (Florence et al., 2007; Javadpour et al., 2007; Civan et al., 2011; Darabi et al., 2012; Shi et al., 2013; Heller et al., 2014). This is also known as the Klinkenberg effect (Klinkenberg, 1941). Slip flow/Knudsen diffusion was pointed out as important in shale reservoir simulation by Sun et al. (2015) where including this mechanism yielded higher recovery vs time. Others have pointed out that slippage could be less significant at high pressure conditions (Darishchev et al., 2013; Rubin et al., 2019). Yet others suggest that the high apparent permeability of shale is not related to slip, but an improper integration of the Navier-Stokes equations (Patzek, 2017; Chen and Shen, 2018; Jin and Chen, 2019).

More conventional mechanisms are also important to account for: Pressure depletion leads to increased effective stresses. Shale can lose porosity and intrinsic permeability upon increased effective stress (Dong et al., 2010). Gas flow at reservoir conditions should account for gas density being pressure dependent, where an equation of state is required to capture deviation from ideal gas behavior. Significant pressure changes may also affect viscosity (Lee et al., 1966).

In this work a 1D model is presented for pressure depletion of gas shale matrix considering mechanisms such as free gas flow, adsorption, compressible real gas, pressure dependent viscosity and apparent permeability, compressible rock with accompanied porosity and permeability alteration. This is representative of production into a hydraulic fracture from matrix in a stimulated reservoir volume. It is shown that the model can be formulated into a nonlinear diffusion equation and solved semi-analytically for early times (before a no-flow boundary is met). We follow the approach of McWhorter and Sunada (1990) who considered oil production by capillary water uptake (spontaneous imbibition). It is shown that gas recovery follows a square root of time profile during the early time period. A scaling time is presented that allows all recovery curves resulting from any input parameter combinations to overlap for early time. Similar scaling in spontaneous imbibition context was presented by Schmid and Geiger, (2012) and Andersen et al. (2020). The model does not account for multiphase flow which can result from the hydraulic fracturing with associated gas relative permeability reduction and capillary blockage (Cheng, 2012), or matrix heterogeneity following such an operation: clay swelling and permeability damage (Holditch, 1979).

The paper is structured as follows: Mass balance and flux relations are derived to give a general description of the shale gas system. This results in a form that can be solved semi-analytically at early times, and a full derivation is provided. Specific relations for the rock and fluid behavior are stated, all of which are expected to cover realistic and important flow mechanisms for single phase flow of shale gas and within the applicability of the analytical solution. The semi-analytical solution is illustrated for several numerical examples and compared to numerical solutions. Scaling is demonstrated and shown to capture all involved mechanisms at early time.
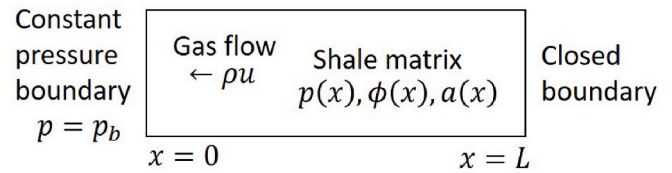

Fig. 1. The system is 1D linear with constant pressure p_b at $x = 0$ and closed boundary at $x = L$.

2. Mathematical model

2.1. Geometry and assumptions

A 1D linear system is considered for flow in shale matrix, see Fig. 1. On one side $x = 0$ the system is open with a fixed pressure p_b, while at the opposite side $x = L$ the system is closed. The initial pressure p_0 is greater than p_b so that gas is produced at times $t > 0$. This represents shale gas production by pressure depletion, from a core sample or matrix surrounding a hydraulic fracture. In the latter case the closed boundary would appear by symmetry between hydraulic fractures and the constant pressure p_b in the fracture is based on good fracture conductivity where the matrix limits the production.

2.2. Mass balance equations

A general mass balance partial differential equation for shale gas accounting for free gas flow, compressibility and adsorption is given by:

$$\partial_t(\varphi\rho + \rho_b a) = -\partial_x(\rho u). \tag{1}$$

where φ is porosity, ρ gas density, a the mass adsorbed gas per mass solid and ρ_b is the (constant) mineral bulk density. φ, ρ and a will be assumed to depend on gas pressure p. The gas flux u is given by Darcy's law with apparent permeability k_a:

$$u = -\left(\frac{k_a}{\mu}\right)\partial_x p \tag{2}$$

Gas density can be expressed in terms of pressure by applying the real gas law:

$$\rho = \frac{M_w}{RT}\frac{p}{z}, \tag{3}$$

M_w is gas molar weight, R the gas constant, T absolute temperature and z gas compressibility factor. It follows that:

$$\partial_t(\varphi\rho + \rho_b a) = \partial_x\left(\rho\frac{k_a}{\mu}\partial_x p\right), \tag{4}$$

We define a variable M as the conserved property in the system. M represents the mass stored due to free and adsorbed gas and pore volume expansion per bulk volume, i.e. a bulk gas density.

$$M(p) = \varphi(p)\rho(p) + \rho_b a(p) \tag{5}$$

$M(p)$ increases monotonously with pressure through the combination of functions porosity, density and adsorption. Typically, they all increase with pressure (or are constant). For methane, a main component of shale gas, adsorption increases with pressure towards a plateau (some gases including CO_2 have similar trend below the critical point, but display reduction of adsorbed mass at higher pressure) (Heller and Zoback, 2014; Klewiah et al., 2020).

From the monotonicity between M and p, any function of pressure can be written as a function of M. We can therefore write the system as a nonlinear diffusion equation:

$$\partial_t M = \partial_x(D(M)\partial_x M), D(M) = \rho\frac{k_a}{\mu}\frac{dp}{dM} \tag{6}$$

$D(M)$ is a diffusion coefficient function of M, with nonnegative values (especially $\frac{dM}{dp} > 0$).

It is assumed the system has uniform initial pressure p_0 and is produced at constant pressure p_b at $x = 0$, while the system is closed at $x = L$. These conditions can be expressed using M:

$$M(x, t = 0) = M(p_0) = M_0, \tag{7}$$

$$M(x = 0, t) = M(p_b) = M_b, \tag{8}$$

$$\partial_x M|_{x=L} = 0. \tag{9}$$

where $M_0 > M_b$ since there is higher pressure and more gas accumulated at the initial state.

2.3. Gas recovery

Gas recovery R_g relative to the amount gas that can be produced from pressure p_0 to p_b is given by:

$$R_g = \frac{1}{(M_0 - M_b)L} \int_{x=0}^{L} [M_0 - M(x)]dx \tag{10}$$

and accounts for compressible free gas in a compressible pore volume and adsorption. This way to represent recovery is useful for scaling purposes and allows comparing different pressure conditions as R_g goes to 1 at p_b. Recovery relative to mass initially in place R_{gIN} is:

$$R_{gIN} = \frac{1}{M_0 L} \int_{x=0}^{L} [M_0 - M(x)]dx \tag{11}$$

Theoretically, if the system depletes to uniform pressures, recovery factors vs pressure are given by:

$$R_g = \frac{M_0 - M(p)}{M_0 - M_b}, R_{gIN} = \frac{M_0 - M(p)}{M_0} \tag{12}$$

2.4. Semi-analytical solution

The system (6) to (9) can be solved semi-analytically for early times, that is, times before the closed boundary affects the system or if this condition is replaced by a semi-infinite boundary:

$$M(x \to \infty, t) = M_0. \tag{13}$$

A solution was presented for a system of this form in the context of counter-current spontaneous imbibition (COUSI) by McWhorter and Sunada (1990). COUSI is a process where capillary forces cause wetting fluid (e.g. water) to be drawn into a porous medium saturated by non-wetting fluid (e.g. oil or gas) and symmetry of the system causes the two phases to flow in opposite directions (Mason and Morrow, 2013; Abd et al., 2019). Asymmetrical systems, e.g. where gravity forces are significant or different phases cover different surfaces, can experience co-current imbibition (Qiao et al., 2018; Andersen et al., 2019a,b). By assuming that the inlet boundary condition could be expressed as a flux proportional to $\sqrt{t}$, McWhorter and Sunada (1990) derived a self-similar solution for water saturation profiles at different times and oil recovery vs time. Schmid et al. (2011) showed that the inlet boundary condition assumption was not a special case, but in line with the system. Andersen et al. (2020) showed that a COUSI system with coupled multiphase flow equations could be solved semi-analytically, extending the solution of McWhorter and Sunada.

The system we now consider has comparable form with the COUSI system studied by McWhorter and Sunada (1990), and the solution adapted to our system will be derived in the following subsections. In terms of their system, our case would correspond to look at the producing non-wetting phase, rather than the invading wetting phase.

Mainly, we will show that the solution can be expressed using a function $F(M)$ such that the position x of a given M at time t is proportional to the square root of time and $F'(M)$ as follows:

$$x(M) = -2AF'(M)t^{\frac{1}{2}}. \tag{14}$$

Pressure distribution follows directly since $p = p(M)$. The constant A and the function $F(M)$ are calculated from the system input parameters. A is, by definition, related to the inlet flux q_0 as:

$$q_0 = -(D(M)\partial_x M)|_{x=0} = -At^{-\frac{1}{2}}, \tag{15}$$

Gas recovery follows the square root of time and can be scaled to a unique curve with time scale τ:

$$R_g = \sqrt{t_D}, t_D = \frac{t}{\tau}, \tau = \left(\frac{(M_0 - M_b)L}{2A}\right)^2. \tag{16}$$

The solution is valid until the critical time t_c when the no-flow boundary is encountered.

$$t_c = \left(\frac{L}{-2AF'(M_b)}\right)^2 \tag{17}$$

Those results and their definitions will be derived in more detail in the following.

2.5. Spatial profiles and cumulative production

We wish to solve the semi-infinite system below:

$$\partial_t M = \partial_x[D(M)\partial_x M], \tag{18}$$

$$M(x, t = 0) = M_0, M(x = 0, t) = M_b, M(x \to \infty, t) = M_0 \tag{19}$$

where $M_0 > M_b$. We recognize a mass flux q in (18) as:

$$q(x, t) = -D(M)\partial_x M, \tag{20}$$

and express the system as:

$$\partial_t M = -\partial_x q, \tag{21}$$

Further, we introduce the boundary condition:

$$q(x = 0, t) = q_0 = -At^{-\frac{1}{2}}, \tag{22}$$

for some constant $A > 0$. It is later demonstrated that this condition does not constrain, but is consistent with, the system. The flux q, both at the inlet and in the system, is negative since mass flows in the negative x-direction. Define a fractional flow function F as the ratio of flux q at a given point x relative to the flux at the inlet q_0:

$$F(x, t) = \frac{q}{q_0} > 0, \tag{23}$$

It is assumed that $F = F(M)$. We substitute this into the flow equation (18):

$$\partial_t M = At^{-\frac{1}{2}}\partial_x F, \tag{24}$$

Now assume that the solution $M(x, t)$ can be expressed only using the variable λ defined by:

$$\lambda = xt^{-1/2} \tag{25}$$

The mass balance equation (24) can then be expressed as:

$$\lambda(M) = -2A\frac{dF}{dM} \tag{26}$$

with boundary conditions:

$$F(M_b) = 1, F(M_0) = 0 \tag{27}$$

The first condition simply states that the value $M = M_b$, found at the

inlet, results in the inlet flux, while the second condition states that there is zero flux in the initial state when $M = M_0$. Using (25) we note that (26) is equivalent to:

$$x(M) = -2AF'(M)t^{\frac{1}{2}} \qquad (28)$$

which states that the position of the solution for any specific value M is proportional to $F'(M)$ and the square root of time. Further, the cumulative production Q is given by integrating the negative flux at the inlet over time:

$$Q = -\int_{t=0}^{t} q_0 dt = 2At^{\frac{1}{2}} \qquad (29)$$

showing that production (or recovery) follows the square root of time. Next, we determine A and $F(M)$ which uniquely determine the solution.

2.6. Calculation of F and A

By the definition of F from (23), F can be written as:

$$F = \frac{q}{q_0} = \frac{D\partial_x M}{At^{-\frac{1}{2}}} \qquad (30)$$

which can be reformulated in the following steps:

$$\frac{D}{AF} = \frac{t^{-\frac{1}{2}}}{\left(\frac{\partial M}{\partial x}\right)} = \frac{\partial\left(xt^{-\frac{1}{2}}\right)}{\partial M} = \lambda'(M) \qquad (31)$$

or simply $\lambda' = \frac{D}{AF}$. Simultaneously, the mass balance equation (26) can be differentiated to give:

$$\lambda' = -2AF'' \qquad (32)$$

Equating the expressions for λ' gives the second order differential

$$G(M) = \frac{1}{2A^2} \int_{\beta=M}^{M_0} \int_{\beta'=\beta}^{M_0} \frac{D(\beta')}{F(\beta')} d\beta' d\beta = \frac{1}{2A^2} \int_{\beta'=M}^{M_0}$$

$$\times \int_{\beta=M}^{\beta'} \frac{D(\beta')}{F(\beta')} d\beta d\beta' = \frac{1}{2A^2} \int_{\beta'=M}^{M_0} (\beta' - M) \frac{D(\beta')}{F(\beta')} d\beta' \qquad (36)$$

The integration constants C_1 and C_2 are determined, based on the inner and initial boundary condition from (27):

$$F(M_0) = 0 + C_1 M_0 + C_2 = 0, \quad F(M_b) = -G(M_b) + C_1 M_b + C_2 = 1 \qquad (37)$$

resulting in:

$$C_1 = \frac{1 + G(M_b)}{(M_b - M_0)}, \quad C_2 = -\frac{1 + G(M_b)}{(M_b - M_0)} M_0 \qquad (38)$$

The updated expressions for F and F' are then:

$$F(M) = \frac{(M - M_0)}{(M_b - M_0)} + \frac{(M - M_0)}{(M_b - M_0)} \frac{1}{2A^2} \int_{\beta'=M_b}^{M_0} \frac{(\beta' - M_b)D(\beta')}{F(\beta')} d\beta'$$

$$- \frac{1}{2A^2} \int_{\beta'=M}^{M_0} (\beta' - M) \frac{D(\beta')}{F(\beta')} d\beta' \qquad (39)$$

$$F'(M) = \frac{1}{2A^2} \int_{\beta'=M}^{M_0} \frac{D(\beta')}{F(\beta')} d\beta' + \frac{1}{(M_b - M_0)}$$

$$+ \frac{1}{(M_b - M_0)} \frac{1}{2A^2} \int_{\beta'=M_b}^{M_0} (\beta' - M_b) \frac{D(\beta')}{F(\beta')} d\beta' \qquad (40)$$

We next require that $F'(M_b) = 0$ to ensure that the nonzero inlet flux (22) is consistent with a nonzero gradient $\partial_x M$ as in (20).

$$F'(M_b) = \frac{1}{2A^2} \int_{\beta'=M_b}^{M_0} \frac{D(\beta')}{F(\beta')} d\beta' + \frac{1}{(M_b - M_0)} + \frac{1}{(M_b - M_0)} \frac{1}{2A^2} \int_{\beta'=M_b}^{M_0} (\beta' - M_b) \frac{D(\beta')}{F(\beta')} d\beta' = 0 \qquad (41)$$

equation:

$$F'' = -\frac{1}{2A^2} \frac{D}{F} \qquad (33)$$

This is integrated directly to give F' and F:

$$F'(\beta) = \int_{\beta'=M_0}^{\beta} F''(\beta') d\beta' + C_1 = \frac{1}{2A^2} \int_{\beta'=\beta}^{M_0} \frac{D(\beta')}{F(\beta')} d\beta' + C_1 \qquad (34)$$

$$F(M) = \int_{\beta=M_0}^{M} F'(\beta) d\beta = -\frac{1}{2A^2} \int_{\beta=M}^{M_0} \int_{\beta'=\beta}^{M_0} \frac{D}{F} d\beta' d\beta + C_1 M + C_2 \qquad (35)$$

C_1 and C_2 are integration constants. The second order integral in (35), termed $G(M)$ is simplified by reversing the order of integration (with corresponding update of integration limits) and then solving the inner integration.

This allows to define A:

$$A^2 = \frac{1}{2} \int_{\beta'=M_b}^{M_0} (M_0 - \beta') \frac{D(\beta')}{F(\beta')} d\beta' \qquad (42)$$

Next, to evaluate F, we note that the expression (39) for F can be simplified by first using that:

$$\beta' - M_b = -(M_0 - \beta') + (M_0 - M_b) \qquad (43)$$

to express the first integral in a form comparable to A, thus canceling the nonintegral terms.

$$F(M) = \frac{1}{2A^2} \int_{\beta'=M_b}^{M_0} (M_0 - M) \frac{D(\beta')}{F(\beta')} d\beta' - \frac{1}{2A^2} \int_{\beta'=M}^{M_0} (\beta' - M) \frac{D(\beta')}{F(\beta')} d\beta' \qquad (44)$$

We express the second integral as a sum of two integrals, where one has limits between M_b and M_0 and collect it with the first integral.

$$F(M) = \frac{1}{2A^2}\left[\int_{\beta'=M_b}^{M_0}(M_0-\beta')\frac{D(\beta')}{F(\beta')}d\beta' + \int_{\beta'=M_b}^{M}(\beta'-M)\frac{D(\beta')}{F(\beta')}d\beta'\right] \qquad (45)$$

Using the definition of A from (42), the final expression for F is obtained:

$$F(M) = 1 - \left[\int_{\beta'=M_b}^{M}(M-\beta')\frac{D(\beta')}{F(\beta')}d\beta'\right] \cdot \left[\int_{\beta'=M_b}^{M_0}\frac{(M_0-\beta')D(\beta')}{F(\beta')}d\beta'\right]^{-1} \qquad (46)$$

Once $F(M)$ had been obtained (from numerical integration), the derivative $F'(M)$ used in calculating spatial profiles (28) was evaluated numerically by a second order approximation.

2.7. Critical time

The solution (28) is valid until the front meets the closed boundary.

$$x(M_b) = -2AF'(M_b)t_c^{\frac{1}{2}} = L \qquad (47)$$

resulting in the critical time t_c denoting this event:

$$t_c = \left(\frac{L}{-2AF'(M_b)}\right)^2 \qquad (48)$$

2.8. Scaling and recovery

We can scale cumulative production against the gas that can be produced by pressure depletion to the boundary pressure to obtain a recovery factor that reaches 1 after sufficient time:

$$R_g = \frac{Q}{(M_0-M_b)L} = \frac{2A}{(M_0-M_b)L}t^{\frac{1}{2}} \qquad (49)$$

Introducing a characteristic time τ, the same recovery is obtained when plotting against scaled time, regardless of initial and boundary pressure:

$$t_D = \frac{t}{\tau}, \tau = \left(\frac{(M_0-M_b)L}{2A}\right)^2 \qquad (50)$$

$$R_g = \sqrt{t_D} \qquad (51)$$

2.9. Consistency in boundary condition

Similar to what was pointed out by Schmid et al. (2011), the flux q can be written as:

$$q(x,t) = -D(M)M'\partial_x\lambda = -D(M)M't^{-\frac{1}{2}}, \qquad (52)$$

such that the flux at $x = 0$ can be written as a constant multiplied by $t^{-\frac{1}{2}}$:

$$q_0 = -\left[D(M_b)M'|_{\lambda=0}\right]t^{-\frac{1}{2}}, \qquad (53)$$

This demonstrates that the boundary condition (22) is not a limitation of the general solution.

2.10. Selected pressure functions

So far, few constraints have been put on the parameters $\varphi, \rho, a, k_a, \mu$ except that they are functions of pressure and can be expressed as functions of M. In this section we select some typical relations used to model gas flow in shales. These choices are established formulations based on correlating large experimental datasets, but can be replaced with more case specific relations. With the following approach any gas composition can be assumed if it can be represented by its molar weight and critical properties and it can be assumed the free and desorbed gas behave similarly.

2.11. Porosity

Porosity is set as a function of pressure according to a standard compressibility formulation:

$$\varphi = \varphi_0\exp(-c_r(p_0-p)) \qquad (54)$$

At the initial pressure p_0, the porosity φ_0 is obtained. At reduced pore pressure, porosity is reduced.

2.12. Adsorption

The mass adsorbed gas per mass solid, a_g, is modeled by a Langmuir isotherm (Langmuir, 1918; Darishchev et al., 2013; Yu and Sepehrnoori, 2014; Jiang and Yang, 2018; Berawala et al., 2019; Rubin et al., 2019):

$$a = a_{max}\frac{p}{p_L+p} \qquad (55)$$

a_{max} is the adsorption capacity (at infinite pressure) and p_L is the gas pressure at which half this capacity is obtained. Other isotherms (such as BET) are also applicable.

2.13. Apparent and intrinsic permeability

Apparent permeability k_a is related to intrinsic permeability k_∞ and Knudsen number K_n according to (Loeb, 1934; Florence et al., 2007; Jiang and Yang, 2018):

$$k_a = k_\infty(1+\alpha_K K_n)\left(1+\frac{4K_n}{1+K_n}\right) \qquad (56)$$

$$\alpha_K = \frac{128}{15\pi^2}\tan^{-1}\left(4K_n^{0.4}\right) \qquad (57)$$

$$K_n = \frac{\lambda}{r} = \frac{\mu Z}{pr}\sqrt{\frac{\pi RT}{2M_w}} \qquad (58)$$

where r is matrix pore radius. In the above, viscosity and gas compressibility factor are functions of pressure: $\mu_g(p), z(p)$. Temperature is assumed constant. The intrinsic permeability k_∞ is given by (Florence et al., 2007; Jiang and Yang, 2018):

$$k_\infty = \frac{r^2}{8}\frac{\varphi}{\tau_f} \qquad (59)$$

We assume rock compressibility (reduced porosity) reduces pore radius and increases formation tortuosity τ_f. The radius-porosity relation is based on a bundle-of-tube approach, while tortuosity is let vary with porosity from a reference value:

$$\frac{\varphi}{\varphi_0} = \left(\frac{r}{r_0}\right)^2, \tau_f = \tau_{f0}\left(\frac{\varphi_0}{\varphi}\right)^{n_\tau} \qquad (60)$$

2.14. Real gas density

To calculate the z-factor and density an equation-of-state (EOS) can be used. The Peng and Robinson (1976) EOS was applied with input of gas critical pressure p_c and temperature T_c and acentric factor ω.

$$z^3 - (1-B)z^2 + (A-3B^2-2B)z - (AB-B^2-B^3) = 0 \qquad (61)$$

$$A = 0.45724\alpha(T_r,\omega)\frac{p_r}{T_r^2}, B = 0.07780\frac{p_r}{T_r}, T_r = \frac{T}{T_c}, p_r = \frac{p}{p_c} \qquad (62)$$

$$\alpha = \left(1+\kappa\left(1-T_r^{0.5}\right)\right)^2, \kappa = 0.37464 + 1.54226\omega - 0.26992\omega^2 \qquad (63)$$

T_r, p_r are reduced temperature and pressure.
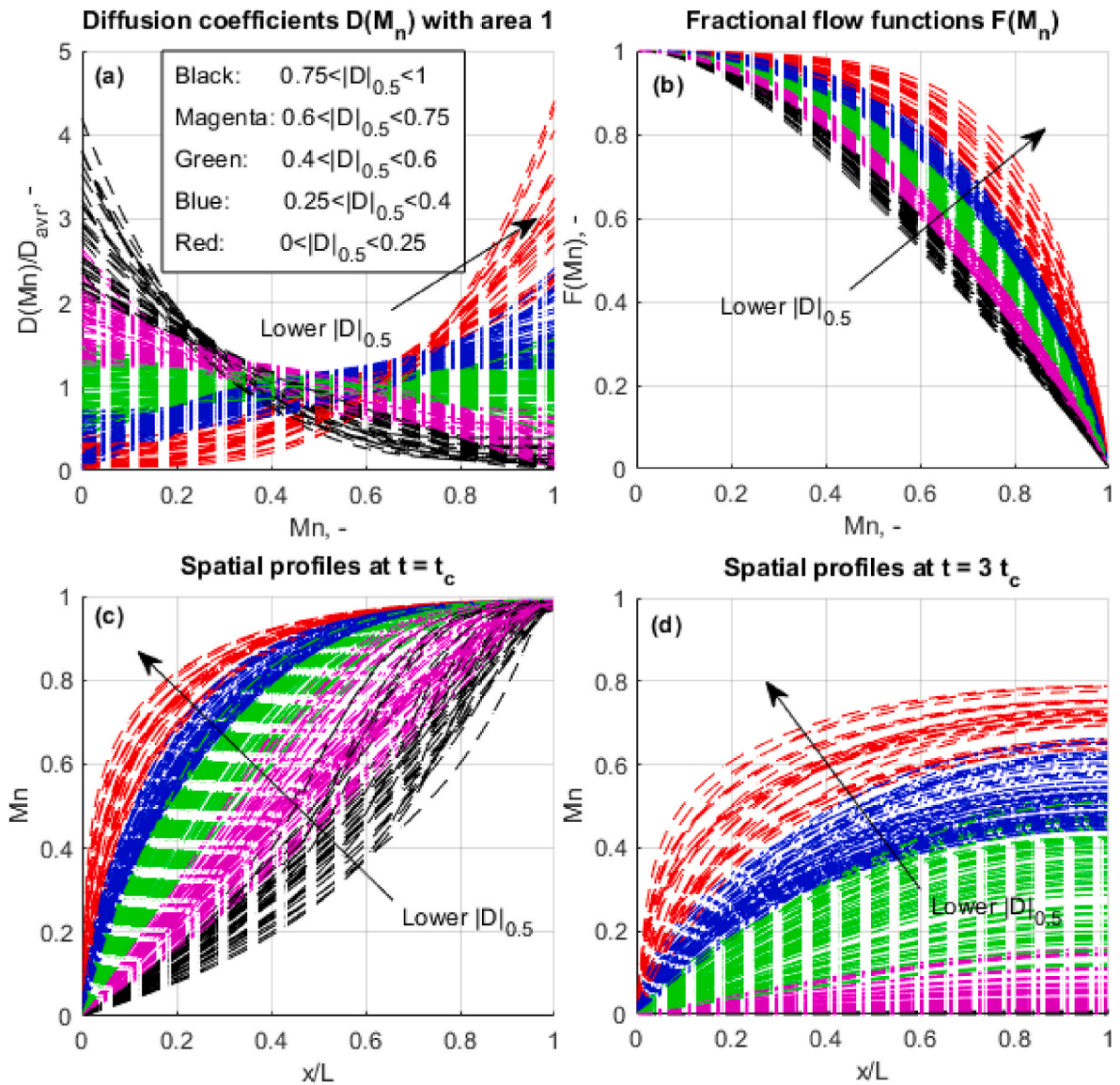
Fig. 2. (a) 250 randomly generated functions representing $D(M_n)$ normalized to an area of 1 (e.g. by dividing by the total area) based on different exponents and end point ratios. The curves are sorted with color according to how much of their area is located between $0 < M_n < 0.5$, denoted $|D|_{0.5}$. (b) The resulting fractional flow functions F. (c) Spatial profiles M_n at the critical time t_c and (d) at $3t_c$.

2.15. Gas viscosity

Gas viscosity was modeled based on Lee et al. (1966):

$$\mu = 10^{-7} K \exp\left[X\left(\frac{\rho}{1000}\right)^Y\right], K = \frac{[9.379 + 0.01607(1000M_w)](1.8T)^{1.5}}{209.2 + 19.26(1000M_w) + (1.8T)},$$

(64)

$$X = 3.448 + \frac{986.4}{(1.8T)} + 0.01009(1000M_w), Y = 2.447 - 0.2224X$$

(65)

Conversion factors are included so that μ, ρ, T, M_w are in SI units.

2.16. Normalized system of equations

We note that by introducing a scaled a normalized bulk gas density M_n with values between 1 (initial high p_0 and M_0) and 0 (final low boundary p_b and M_b) as:

$$M_n = \frac{M - M_b}{M_0 - M_b}$$

(66)

equations (6)–(9) can be turned into:

$$\partial_t M_n = \partial_x(D(M_n)\partial_x M_n),$$

(67)

$$M_n(x, t=0) = 1, M_n(x=0, t) = 0, \partial_x M_n|_{x=L} = 0.$$

(68)

This notation is useful since it shows that the main parameter that affects the solution behavior is the nonlinear diffusion coefficient $D(M_n)$ evaluated over the interval $0 < M_n < 1$. System specific solutions can be obtained by reversing the scaling.

3. Results

3.1. Numerical implementation

The semi-analytical solution was implemented by first determining A and $F(M)$ numerically from (42) and (46), respectively. Iteration was required since F is expressed implicitly in (46) as an integral of itself. Then the expressions (28), (48), (50) and (51) were applied directly. $N_m = 100$ equally spaced points of M were used to evaluate F and positions $x(M)$. The system was also solved numerically by a fully implicit
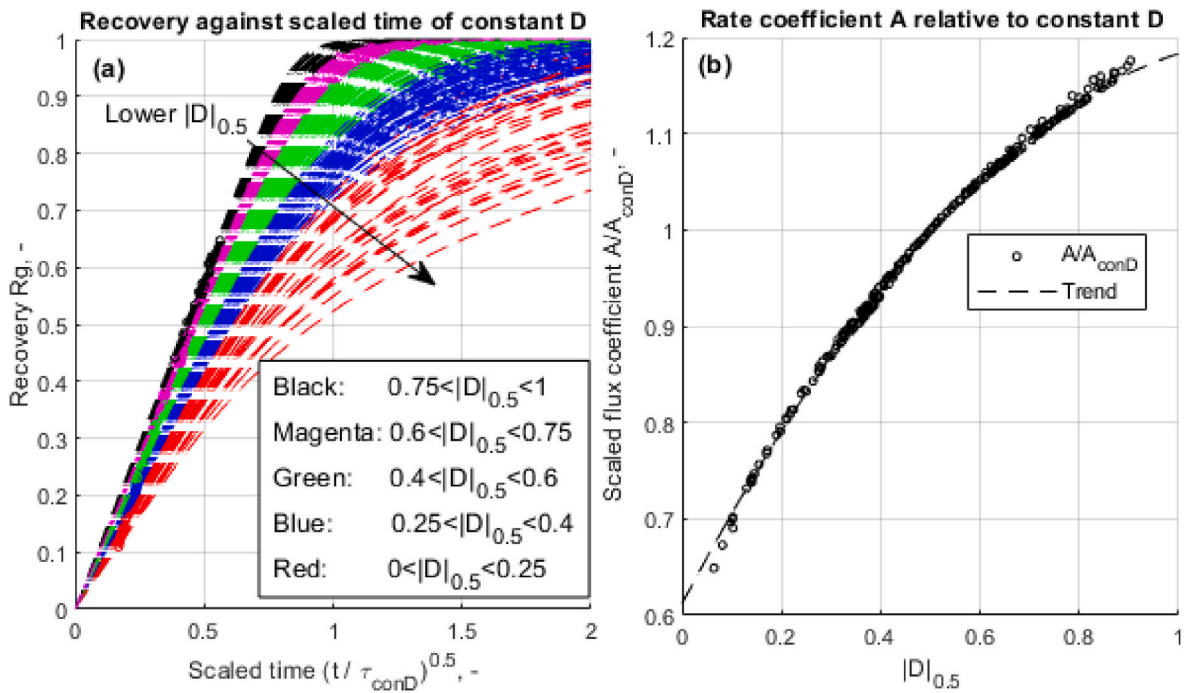
Fig. 3. Recovery plotted against time scaled with the time scale τ_{conD} of a case with constant diffusion coefficient (a). The curves are based on the 250 randomly generated functions $D(M_n)$ and are sorted with color according to $|D|_{0.5}$. In (b), the flux coefficient for each case divided by the flux coefficient of a case with constant D is plotted against $|D|_{0.5}$.

approach, in the case of a closed boundary at $x = L$. The discretization approach is outlined in the **Appendix**. $N_x = 150$ equally spaced grid cells were used and 50 time steps per unit of $\sqrt{\frac{t}{t_c}}$.

3.2. The impact of diffusion coefficient shape on system behavior

Before exploring a specific shale system we will consider that in equations (67) and (68) it is only the nonlinear diffusion coefficient $D(M_n)$ evaluated over the interval $0 < M_n < 1$ which determines the solution. Combinations of parameters and mechanisms specific to a porous medium may result in different such functions and we will explore those relations in the subsequent sections. Here we will first consider varying the shape of the $D(M_n)$ function using simple functions and study the impact on the solution. For symmetry, we let $D(M_n)$ take either of the two following forms:

$$D(M_n) = D_1(M_n)^n + D_2, \quad (0 < M_n < 1) \tag{69}$$

$$D(M_n) = D_1(1 - M_n)^n + D_2, \quad (0 < M_n < 1) \tag{70}$$

The parameters D_1, D_2 are set such that the integral of the function equals 1 and we define the ratio r_{EP} as the ratio of the end points. We thus require:

$$\int_{M_n=0}^{1} D(M_n)dM_n = 1, \quad r_{EP} = \frac{D(1)}{D(0)} \tag{71}$$

The area of 1 can be justified by studying the solution relative to if the coefficient was constant. With the constraints (71), equations (69) and (70) turn into (72) and (73) respectively below:

$$D(M_n) = \frac{n+1}{n+r_{EP}}[(r_{EP}-1)(M_n)^n + 1], \quad (0 < M_n < 1) \tag{72}$$

$$D(M_n) = \frac{1+n}{1+r_{EP}n}[(1-r_{EP})(1-M_n)^n + r_{EP}] \tag{73}$$

For nonnegative values of parameters r_{EP}, n these functions are

nonnegative. A useful parameter characterizing each function, is the area between $M_n = 0$ and 0.5, which is denoted $|D|_{0.5}$ and defined by:

$$|D|_{0.5} = \int_{M_n=0}^{0.5} D(M_n)dM_n \tag{74}$$

For the two functions (72) and (73), the areas between 0 and 0.5 can be calculated as (75) and (76), respectively:

$$|D|_{0.5} = \frac{0.5}{n+r_{EP}}[(r_{EP}-1)0.5^n + (n+1)] \tag{75}$$

$$|D|_{0.5} = \frac{1-r_{EP}}{1+r_{EP}n}[1 - 0.5^{n+1}] + r_{EP}\frac{1+n}{1+r_{EP}n}0.5 \tag{76}$$

In the following examples, 250 functions $D(M_n)$ were randomly generated with the exponent n uniformly selected between 0.5 and 4, and the end point ratio r_{EP} loguniformly selected between 0.01 and 100. The two functions (72) and (73) were selected evenly.

The functions $D(M_n)$ are shown in Fig. 2a, colored according to the value of $|D|_{0.5}$. The functions with high $|D|_{0.5}$ values are shifted to the left and those with low values are shifted to the right. Due to the nonlinearity of the functions, there is some overlap. The calculated fractional flow functions $F(M_n)$ are shown in Fig. 2b where we see a clear trend according to the values of $|D|_{0.5}$: the functions $D(M_n)$ with low $|D|_{0.5}$ have values of F shifted closer to 1 (before going to 0 at high M_n) compared to the functions $D(M_n)$ with high $|D|_{0.5}$ where the functions F seem to approach a straight line from 1 to 0.

The profiles $M_n\left(\frac{x}{L}\right)$ are shown at t_c (when the profile meets the no-flow boundary) in Fig. 2c and $3t_c$ in Fig. 2d. It is seen that the cases with low $|D|_{0.5}$ have profiles with high M_n at the critical time t_c when $M_n = 1$ reaches the no-flow boundary. This can be related to the F function which has low derivatives $F'(M_n)$ for low M_n and these derivatives determine the spatial profile, see (28). The cases with higher $|D|_{0.5}$ have generally lower M_n profiles at the critical time, which can be related to the more similar derivatives F'. The same trends follow at later

times.

Recovery R_g for the mentioned cases is plotted against scaled time in Fig. 3a where the time is divided by the time scale τ_{conD} calculated for a case where the diffusion coefficient is constant equal to 1. The constant D case is in the green group where $0.4 < |D|_{0.5} < 0.6$, since $|D|_{0.5} = 0.5$ for that case. Cases with low $|D|_{0.5}$ (where the coefficient is skewed towards high M_n) yield slower recovery compared to the uniform case, while the cases with high $|D|_{0.5}$ (where the coefficient is skewed towards low M_n) yield faster recovery than the uniform case. The trend in slower recovery with lower $|D|_{0.5}$ seems to be valid for both early and late time, i.e. both when the curves are linear with the square root of time and after.

In Fig. 3b the flux coefficient A is calculated for each case and divided by the value of A for the case where D is constant equal to 1. Based on the 250 points, a very clear trend is seen: higher $|D|_{0.5}$ leads to higher A and opposite, meaning that if the diffusion coefficient D is shifted to the low M_n interval, the recovery will be faster than if D was constant with same total area. Note that the data pass through A/A_{conD} at $|D|_{0.5} = 0.5$ as expected. Looking at the scale of the results, the change in flux coefficient by modifying the diffusion coefficient shape seems to be within a factor of 0.65–1.15 time that of a constant coefficient. A trend line was regressed through the points using a second order polynomial:

$$\frac{A}{A_{conD}} = -0.404|D|_{0.5}^2 + 0.975|D|_{0.5} + 0.612, \ (R^2 = 0.9985, \ RMSE = 0.0045)$$

(77)

The high coefficient of determination $R^2 = 0.9985$ and low root mean square error ($RMSE = 0.0045$) indicate strong correlation. This correlation can be used to quickly predict the flux coefficient A for any diffusion coefficient.

Scaled recovery is also shown in Fig. 4a where the time is scaled against τ calculated for each individual case. In accordance with theory, all recovery curves fall on the same straight line by this scaling at early time. This is an exact result, while the correlation (77) only is based on one effective parameter from the nonlinear diffusion coefficient. The critical time and corresponding critical time recovery are marked for each curve with a circle to illustrate where the semi-analytical solution ceases to be valid. We see that the critical time recovery follows the pattern of $|D|_{0.5}$, where higher $|D|_{0.5}$ corresponds to higher critical time recovery. The red cases with $0 < |D|_{0.5} < 0.25$ have critical time recovery as low as 0.1 to 0.20, while the black cases with $0.75 < |D|_{0.5} < 1$ have critical time recovery around 0.45 to 0.65. Although the semi-analytical solution ceases to be valid at these times, it appears that recovery can be much higher before the solutions deviate significantly. For
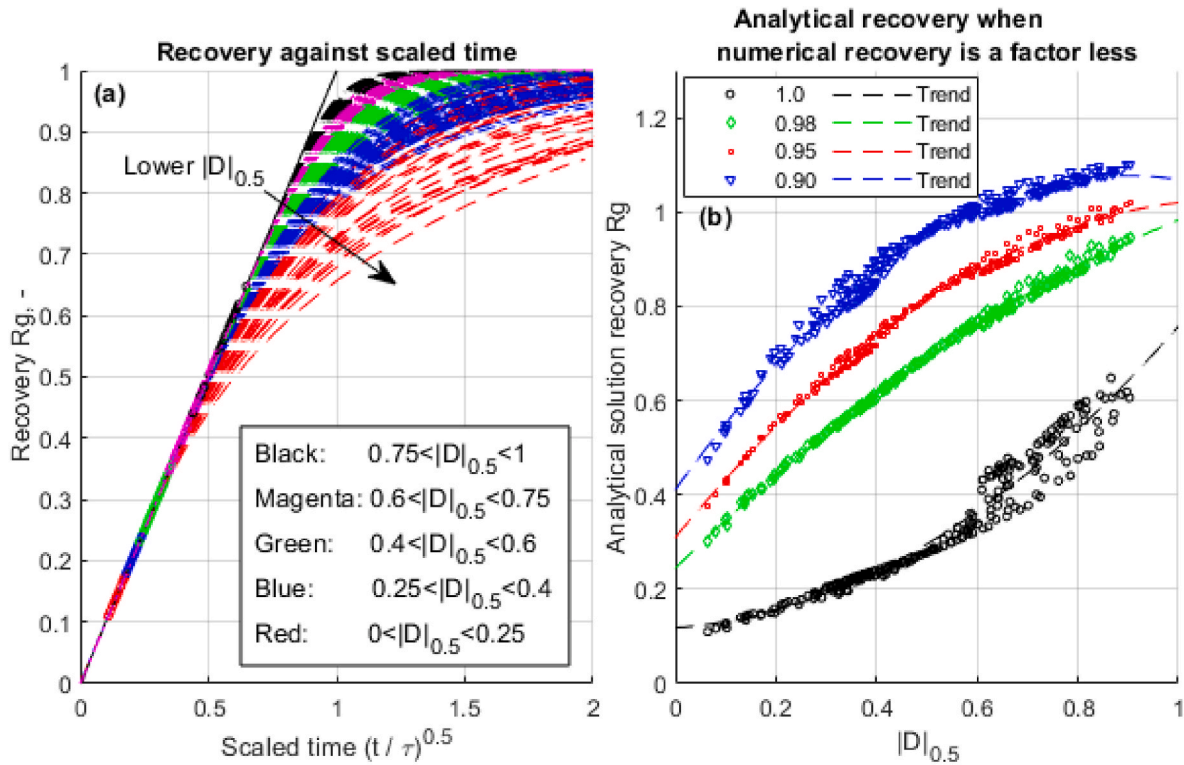
Fig. 4. Recovery plotted against scaled time using the time scale τ calculated for each individual case (a). The recovery curves are based on the 250 randomly generated functions $D(M_n)$ and are sorted with color according to $|D|_{0.5}$. The black solid line indicates the extrapolated straight line of the semi-analytical solution $R_g = \left(\frac{t}{\tau}\right)^{0.5}$. In (b), the recovery of the semi-analytical solution at the critical time (black points), and when the numerical solution is 0.98 times (green points) the semi-analytical solution, 0.95 times (red points) and 0.90 times (blue points).

$$\left(R_{gAn}\right)_{\frac{An}{Num}=1.0} = 0.570|D|_{0.5}^2 + 0.0695|D|_{0.5} + 0.118, \ \left(R^2 = 0.9557, \ RMSE = 0.0288\right)$$

(78)

$$\left(R_{gAn}\right)_{\frac{An}{Num}=0.98} = -0.310|D|_{0.5}^2 + 1.05|D|_{0.5} + 0.244, \ \left(R^2 = 0.9979, \ RMSE = 0.0070\right)$$

(79)

$$\left(R_{gAn}\right)_{\frac{An}{Num}=0.95} = -0.585|D|_{0.5}^2 + 1.30|D|_{0.5} + 0.309, \ \left(R^2 = 0.9947, \ RMSE = 0.0106\right)$$

(80)

$$\left(R_{gAn}\right)_{\frac{An}{Num}=0.90} = -0.830|D|_{0.5}^2 + 1.49|D|_{0.5} + 0.410, \ \left(R^2 = 0.9860, \ RMSE = 0.0164\right)$$

(81)

Table 1

Reference input parameters for simulation. [1]Data from Yu and Sepehrnoori (2014) matched to or representative of Marcellus shale.

[1]φ_0	0.065[1]	ρ_b	$2.46 \cdot 10^3 \frac{kg}{m^3}$	T_c	190.56 K
[1]p_0	$33 \cdot 10^6$ Pa	[1]a_{max}	$0.00370 \frac{kg}{kg}$	p_c	4.599 MPa
[1]p_b	$3.7 \cdot 10^6$ Pa	[1]p_L	$3.5 \cdot 10^6$ Pa	ω	0.011
[1]L	15 m	r_0	12 nm	R	8.314 J/K/mol
[1]T	352 K	τ_{f0}	2	M_w	$16.04 \cdot 10^{-3}$kg/mol
[1]c_r	$1.5 \cdot 10^{-10}$ Pa^{-1}	n_τ	3		
[1]$k_\infty(p_0)$	585 nD	$\mu_g(p_0)$	0.024 cP		

example, the red cases appear to deviate from the straight line at recoveries between 0.4 and 0.5, which is an interval of 0.2 units higher than where the critical time recoveries were located. For the black cases, the deviation is noticeable at recovery points 0.7 to 0.9 which is an interval of 0.25 recovery units higher than the critical points. This means that the semi-analytical solution is a good approximation also after the critical time.

Some more investigation was made regarding the difference between the semi-analytical and numerical solutions. In Fig. 4b we plot the recovery of the semi-analytical solution, i.e. $\sqrt{t/\tau}$, at the critical time (the last time when the two solutions are exactly identical), and when the numerical solution is 0.98 times, 0.95 times or 0.90 times the recovery of the numerical solution. These results are plotted as function $|D|_{0.5}$. We see that the recovery for each of these conditions is largely controlled by
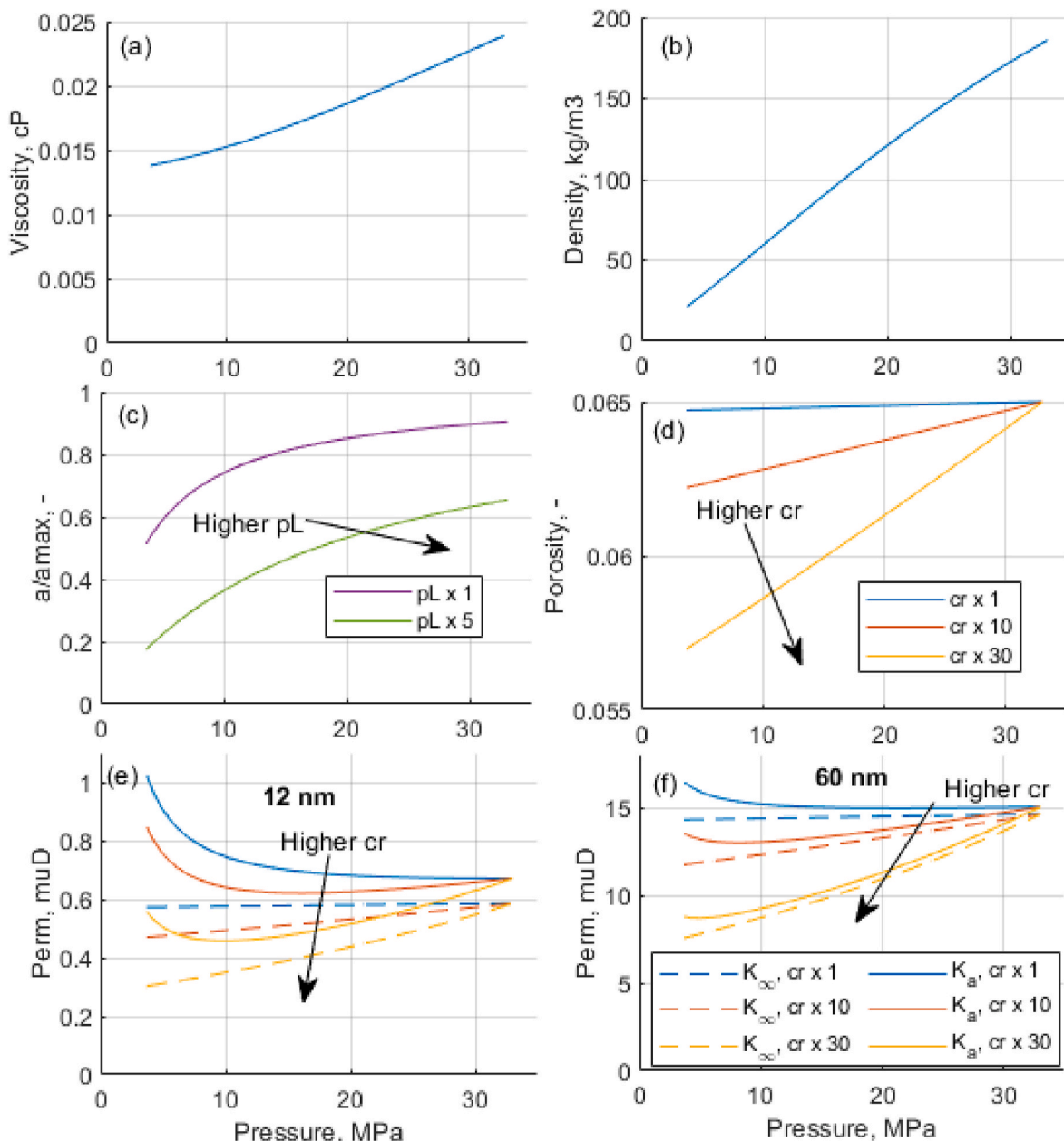
Fig. 5. Input functions plotted over the considered pressure range including gas viscosity (a), gas density (b), adsorption relative to max capacity (at infinite pressure) (c), porosity relative to initial porosity (d) and in the last two figures intrinsic permeability (dashed lines) and apparent permeability (full lines) are shown for 12 nm (e) and 60 nm (f) initial pore radius. Porosity reduction and permeabilities depend on compressibility (3 values are used; 1, 10 or 30 times the reference compressibility). The adsorption isotherm is shown for the reference Langmuir pressure and a 5 times higher value.
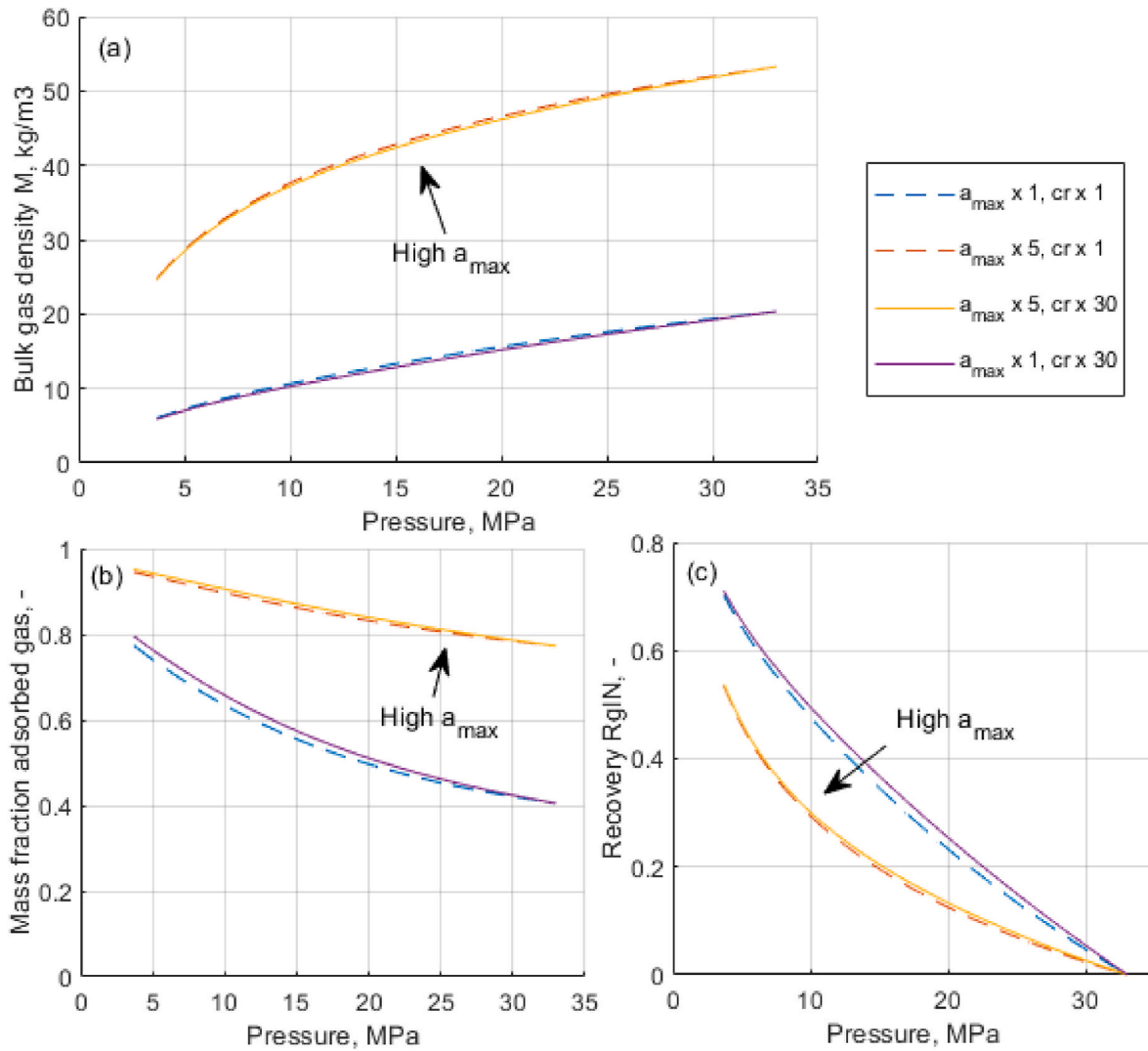
Fig. 6. The bulk gas density $M = \varphi\rho + \rho_b a$ (a), the mass fraction adsorbed gas $\frac{\rho_b a}{M}$ (b) and gas recovery (c) R_{gIN} relative to gas initially in place, all plotted against pressure. The adsorption capacity and rock compressibility are varied as indicated from the reference values. The curves do not depend on initial radius when same initial porosity is assumed.

$|D|_{0.5}$ in monotonous ways with little scatter. Regression lines are summarized in (78) to (81). For cases with larger $|D|_{0.5}$ the semi-analytical solution is valid to higher recovery; ranging from recovery as low as 0.1 when $|D|_{0.5} \approx 0.1$ to as high as 0.6 when $|D|_{0.5} \approx 0.9$. Considering the curves representing where the numerical solution is slightly less than the semi-analytical solution (the semi-analytical solution overestimates recovery), higher recovery can be obtained with low error for cases with higher $|D|_{0.5}$. We also see that for the curve where the numerical recovery is 0.98 times the semi-analytical solution, recovery is ~0.2 units higher than the recovery at the critical time (where the solutions are identical) for low $|D|_{0.5}$, up to 0.4 units higher for intermediate $|D|_{0.5}$ and 0.3 units higher at high $|D|_{0.5}$. The curve for recovery values of the analytical solution when the numerical solution are 0.95 times lower is roughly 0.1 unit higher than the curve with factor 0.98. Summarized, we see that the semi-analytical solution is a good approximation of the numerical solution at late times in cases of high $|D|_{0.5}$, which also corresponds to the cases where the semi-analytical solution is identical to the numerical for a relatively high recovery during the early time.

3.3. Input parameters for a shale system

Reference input parameters for pressure, porosity, permeability, adsorption, temperature and more are shown in Table 1 and are based on Marcellus shale as listed by Yu and Sepehrnoori (2014). Methane composition was assumed to model gas density and viscosity as this is the main constituent in shale gas (Darishchev et al., 2013; Cao et al., 2016).

In Fig. 5 several properties are plotted against the considered pressure range 3.7–33 MPa (well pressure to initial pressure). Viscosity increases with pressure from 0.014 to 0.024 cP. Density increases with increasing pressure from ~20 to ~180 kg/m3, a significant factor of 9. The adsorption, relative to the capacity at infinite pressure is also plotted. At initial pressure ~0.9 of this capacity is used, while at well pressure ~0.5 of the capacity is used. After pressure depletion, 0.5/0.9 = 0.56 of the adsorbed gas therefore remains. For a 5 times higher Langmuir pressure p_L than the reference, less gas is adsorbed in the given pressure range, but more of the initial adsorbed gas can be desorbed: only a fraction 0.18/0.65 = 0.28 of the initial adsorbed gas is left after depletion.

Functions depending on more parameters than pressure are also shown in Fig. 5. Porosity reduces more on pressure depletion at high

Table 2

List of cases and how their parameters have been varied: All the values are factors compared to the reference value. In each example, only one parameter is varied relative to the reference case.

Compressibility	Adsorption capacity	Boundary pressure	Initial pore radius	Length	Langmuir pressure
c_r	a_{max}	p_b	r_0	L	p_L
1, 10, 30	0.35, 1, 5	1, 2, 3	1, 2, 5	0.5, 1, 2	1, 2, 5

compressibility. The reference compressibility does not affect porosity much, while a 30 times higher compressibility reduces porosity from 0.065 to ~0.057 (12% reduction). The same initial porosity is used regardless of initial pore radius.

The reduced porosity affects intrinsic permeability and apparent permeability. Higher compressibility reduces porosity and pore radius

with pressure and thus also intrinsic permeability. Low pore radius and low pore pressure increases the difference between intrinsic (dashed lines) and apparent (full lines) permeability. The permeabilities also depend strongly on the initial pore radius and are greatly increased by higher initial radius (60 instead of 12 nm). At large (initial) radii the difference between apparent and intrinsic permeability is less than at low radii.

In Fig. 6a, b and c, bulk gas density M, mass fraction adsorbed gas $\frac{\rho_b a}{M}$ and gas recovery R_{gIN} relative to gas initially in place, respectively, are plotted against pressure. Adsorption capacity a_{max} and rock compressibility c_r are varied. As seen in Fig. 6a, M, which equals $\varphi \rho + \rho_b a$, increases monotonously with pressure, as is required to express functions of pressure to functions of M. When adsorption capacity a_{max} increases, M increases significantly since more adsorbed gas is in the system. Higher pore compressibility does not affect adsorbed mass or initial free mass (by assumption), but reduces the space for free gas upon pressure depletion through the porosity. The effect of pore compressibility on M

Fig. 7. The role of compressibility c_r (in factors times the reference value) on (a) $D(M)$, (b) $F(M)$, (c) recovery R_{gIN} vs time, (d) normalized recovery R_g vs square root of time, spatial profiles of M_n at (e) $t = t_c$ and (f) $t = 9t_c$. In the recovery plots dashed lines indicate the semi-analytical solution and the red circle the point where it ceases to be valid. In the spatial plot at $t = t_c$, crosses indicate the semi-analytical solution.
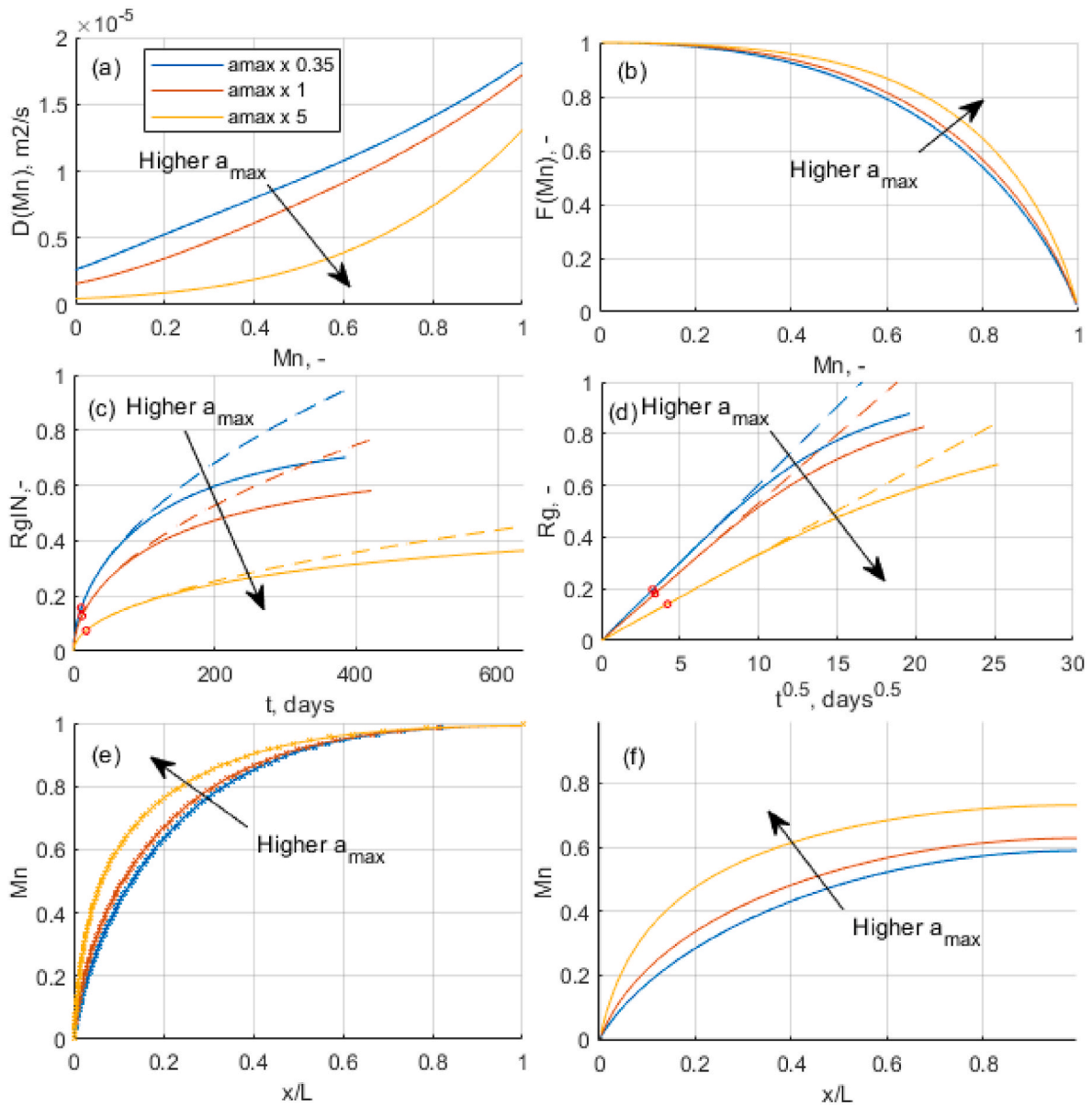
Fig. 8. The role of adsorption capacity a_{max} (in factors times the reference value) on (a) $D(M)$, (b) $F(M)$, (c) recovery R_{gIN} vs time, (d) normalized recovery R_g vs square root of time, spatial profiles of M_n at (e) $t = t_c$ and (f) $t = 9t_c$. In the recovery plots dashed lines indicate the semi-analytical solution and the red circle the point where it ceases to be valid. In the spatial plot at $t = t_c$, crosses indicate the semi-analytical solution.

is small (the curves with high and low c_r are very similar) and most of the reduction in M with pressure depletion is by gas expansion and desorption. We can also see in Fig. 6a that the end points of M (M_0 and M_b) vary with the adsorption and compressibility parameters, even for the same initial and boundary pressure. Clearly also variations in p_0 and p_b affect M_0 and M_b, respectively. In later results, we will therefore use the normalized bulk gas density M_n from (66) with values between 1 (initial high p_0 and M_0) and 0 (final low boundary p_b and M_b). In Fig. 6b it is seen that higher a_{max} increases the adsorbed gas fraction. Higher compressibility reduces the pore space for free gas at low pressure and thus increases the adsorbed fraction more than a low compressibility would. Finally, in Fig. 6c, higher adsorption capacity reduces recovery that can be obtained at a given pressure since gas desorption is less sensitive at higher pressures than low. Note that the above plots do not depend on the value of initial pore radius if initial porosity is assumed the same. We also remark that although compressibility does not seem to affect mass parameters as above, permeability and porosity vary and can give noticeable transient impacts.

3.4. Sensitivity analyses

In this section we systematically vary input parameters around the reference case to investigate the impact on:

- the diffusion coefficient D against M_n,
- the flow function F against M_n,
- recovery R_{IN} vs time t,
- normalized recovery R_g vs $\sqrt{t}$,
- spatial distributions of M_n against $\frac{x}{L}$.

Recovery curves are calculated based on both the numerical (full lines) and semi-analytical (dashed lines) solutions, where the critical time t_c at which the semi-analytical solution becomes invalid is marked (red circle). Each recovery curve is calculated until $t = 36t_c$ (i.e. $\sqrt{t/t_c} = 6$). The spatial distributions are plotted at times $t = t_c$ and at $t = 9t_c$ (i.e. $\sqrt{t/t_c} = 3$). The times were based on that there is $\sqrt{t/t_c}$ times more mass
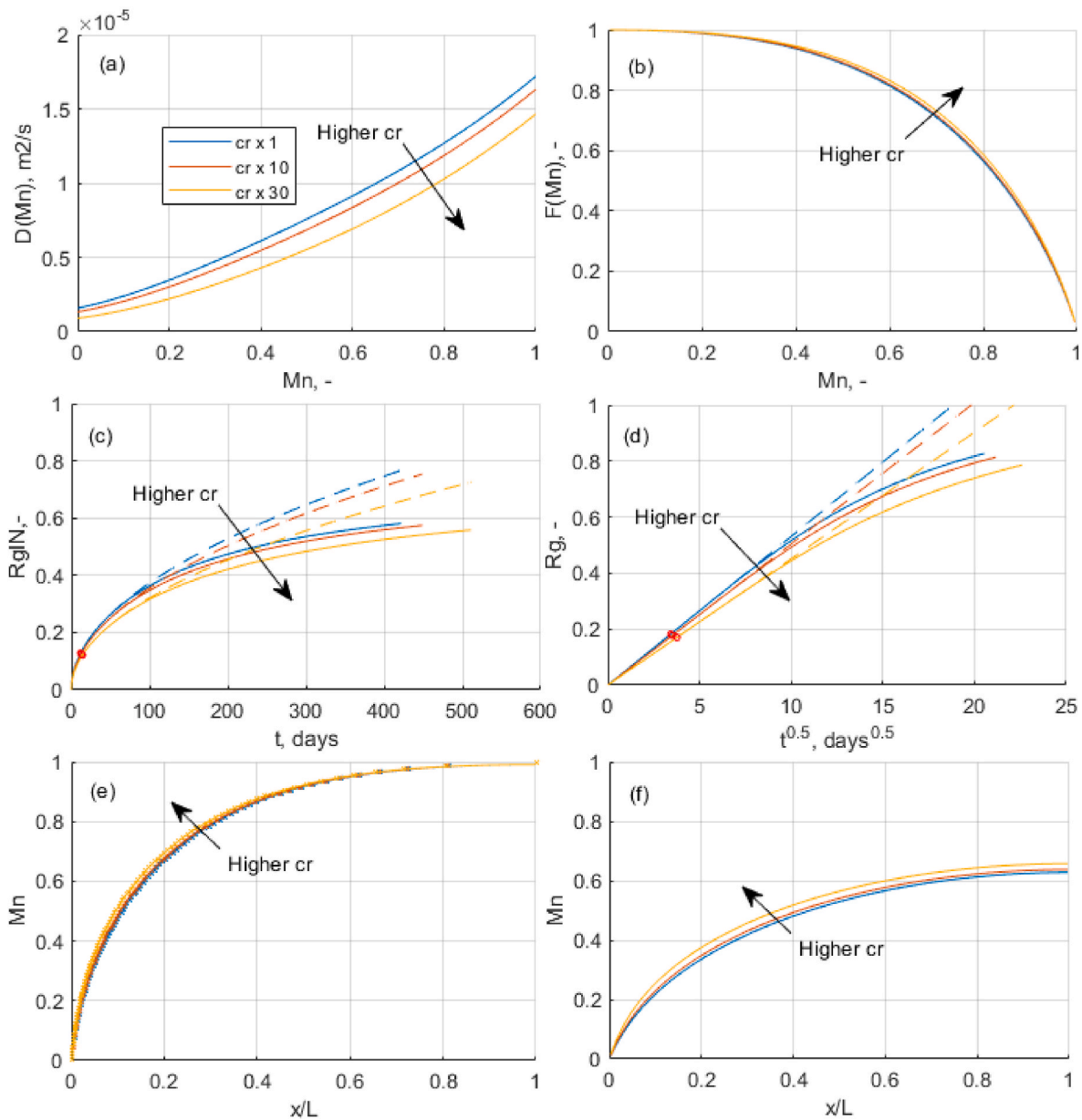
Fig. 9. The role of boundary pressure p_b (in factors times the reference value) on (a) $D(M)$, (b) $F(M)$, (c) recovery R_{gIN} vs time, (d) normalized recovery R_g vs square root of time, spatial profiles of M_n at (e) $t = t_c$ and (f) $t = 9t_c$. In the recovery plots dashed lines indicate the semi-analytical solution and the red circle the point where it ceases to be valid. In the spatial plot at $t = t_c$, crosses indicate the semi-analytical solution.

produced at t than at t_c, had square root of time recovery continued. In Table 2 the cases are summarized. Note that one of the six parameters are varied from the reference case as indicated in the table, while holding all other parameters fixed.

The impact of the parameter variations is illustrated in Fig. 7 to Fig. 12 for each parameter. Before investigating the role of each parameter, we make some general observations from the figures:

- The diffusion coefficient $D = \rho \frac{k_a}{\mu} \frac{dp}{dM}$ is positive (all the involved factors are positive) and appears to increase with M, typically by an order of magnitude from the lowest to highest M, see Figs. 7a to 12a. For the reference case (with ~600 nD permeability) the diffusion coefficient is in the range $10^{-6} - 10^{-5}$ m^2/s. In that case, the gas density increases by a factor ~9 from the lowest to highest pressure, see Fig. 5b. However, inverse viscosity and apparent permeability decrease with pressure, see Fig. 5a and e. Considering the shape of $M(p)$ in Fig. 6a we see that $\frac{dM}{dp}$ (the slope of M vs p) decreases with pressure, such that $\frac{dp}{dM}$ increases with pressure. If free gas is dominant, an approximation with the ideal gas law results in a constant $\frac{dp}{dM}$,

while the change in $\frac{dp}{dM}$ is more significant with high adsorbed gas content. Significant changes in permeability due to compressibility will shift the apparent permeability function to increase more strongly with pressure.

- Similar to some of the examples in Fig. 2 it seems that the functions $D(M_n)$ are monotonous, positive and increasing. From visual inspection, $|D|_{0.5} \sim 0.2 - 0.4$, but cases with higher fraction of adsorbed gas and with permeability more significantly increasing with pressure (due to compressibility) can shift the D functions more, yielding even lower $|D|_{0.5}$. From Fig. 4b we can thus expect the semi-analytical solution to be valid to relatively low recoveries of 0.2–0.25, although being a good approximation for recoveries up to a range 0.45–0.6 (when the numerical solution is a factor 0.98 of the semi-analytical solution recovery).

- The fractional flow function is defined as the flux at a given point divided by the flux at $x = 0$. As seen in Figs. 7b to 12b, F decreases from $F(M_n = 0) = 1$ to $F(M_n = 1) = 0$ meaning the flux is highest at the open face and decreasing into the system. In other words there is net flow towards the open face.

Fig. 10. The role of initial radius r_0 (in factors times the reference value) on (a) $D(M)$, (b) $F(M)$, (c) recovery R_{gIN} vs time, (d) normalized recovery R_g vs square root of time, spatial profiles of M_n at (e) $t = t_c$ and (f) $t = 9t_c$. In the recovery plots dashed lines indicate the semi-analytical solution and the red circle the point where it ceases to be valid. In the spatial plot at $t = t_c$, crosses indicate the semi-analytical solution.

- The flow function F is flat at $M = 0$ and becomes steeper with higher M, meaning higher M travel with higher speed into the system. M_0 has highest speed and M_b has zero speed.

- Recovery follows exactly a profile that is linear with the square root of time until the critical time t_c, indicated by red circle, see Figs. 7d to 12d. Recovery then is usually around $R_g(t_c) \approx 0.20$, which is in line with the results in Fig. 4b for the low $|D|_{0.5}$ cases. Square root of time recovery is however a very good approximation even until $\sqrt{t/t_c} = 2 - 2.5$, i.e. times up to 6 times longer than when they match exactly. Similar observations were made by March et al. (2016). Recovery is then around $R_g(2.5t_c) \approx 0.45$. In other words, the semi-analytical solution predicts recovery accurately until roughly half the producible gas is recovered at given pressure conditions.

- For times $t \gg 6t_c$ the numerical solution always falls visibly below the extrapolated analytical solution at late times, i.e. recovery goes slower than by the square root of time, see Fig. 7c and d to Fig. 12c and d.

- All spatial profiles of $M_n\left(\frac{x}{L}\right)$ exactly reach the noflow boundary at $t = t_c$. There is perfect overlap between the numerical (full lines) and semi-analytical solution (crossed points) at that time (see Figs. 7e to 12e) and earlier times (not shown). At later times the semi-analytical solution is not valid and only numerical profiles are shown (Figs. 7f to 12f).

Increased *rock compressibility* c_r, see Fig. 7, reduces D, primarily because permeability is reduced and $\frac{dM}{dp}$ is increased in (6) (M reduces more by greater pore volume reduction through the porosity). The shape of D remains similar (not identical), hence the impact on F and the spatial profiles is small, although we see that F is lifted for a given M_n with higher compressibility. Recovery is delayed by the permeability reduction (falling from ca 0.7 μD at reference to 0.5 μD with 30x higher compressibility, see Fig. 5). After 400 days $R_g \approx 0.80$ with low compressibility and 0.70 with high compressibility.

Adsorption capacity a_{max} is varied in Fig. 8 to give initial adsorbed mass fractions $\frac{\rho_b a}{M}$ equal to 0.19, 0.40 and 0.77, consistent with reported
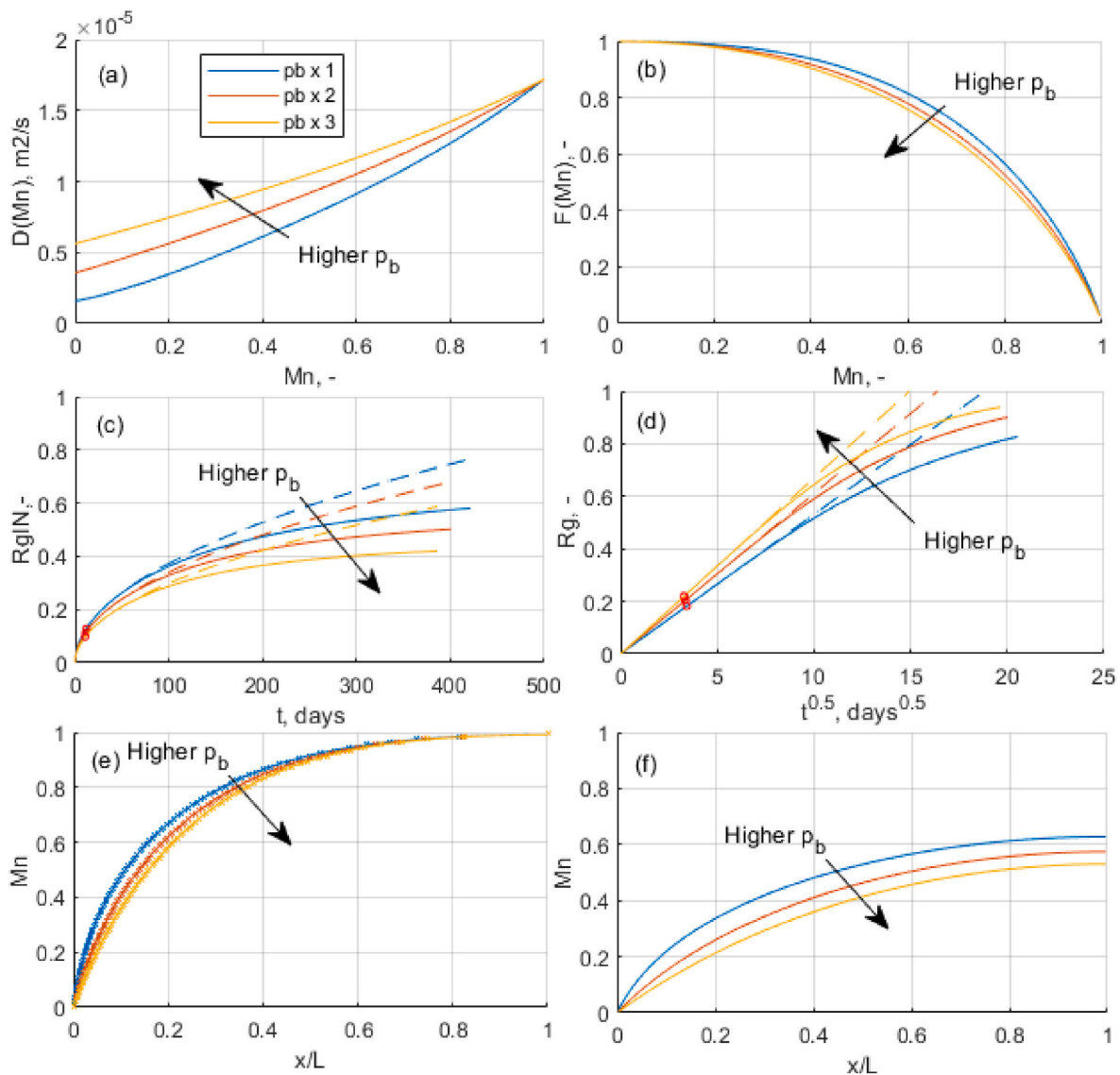
Fig. 11. The role of system length L (in factors times the reference value) on (a) $D(M)$, (b) $F(M)$, (c) recovery R_{gIN} vs time, (d) normalized recovery R_g vs square root of time, spatial profiles of M_n at (e) $t = t_c$ and (f) $t = 9t_c$. In the recovery plots dashed lines indicate the semi-analytical solution and the red circle the point where it ceases to be valid. In the spatial plot at $t = t_c$, crosses indicate the semi-analytical solution.

ranges in the literature (Kuuskraa et al., 1985; Curtis, 2002). Increased values of a_{max} reduces D since $\frac{dM}{dp}$ is increased in (6). At low adsorption capacity, free gas is dominant. If gas is ideal and porosity and permeability are constant, $M \propto p$, i.e. $\frac{dM}{dp} = $ constant and $D \propto M$. A close to linear trend of $D(M)$ is also seen for low capacity, while at high adsorption capacity the trend D vs M_n is more nonlinear. Adsorption delays the velocity of a given pressure (Berawala et al., 2019). Since little desorption happens at high pressures (where the isotherm is flatter, see Fig. 5), high pressures are less delayed by adsorption than low pressures (the diffusion coefficient is less reduced). This is reflected in the F function which is elevated with higher capacity and thus steeper at higher M and the corresponding spatial profiles where low M have reached a shorter distance than high M when M_0 is at $x = L$. The recovery R_g at t_c (see red circles) is thus lower at greater adsorption capacity.

The _boundary pressure_ p_b is varied in Fig. 9. Higher p_b shifts the range of M to high values, where also high values of D are found. A shorter range of D is therefore spanned over M_n starting from the same M_0, making D more flat. The different M travel with more similar speeds and

increases the recovery at t_c. This is consistent with the trends seen for a shift towards higher $|D|_{0.5}$. The generally higher D gives faster recovery R_g of the recoverable gas in the considered pressure interval. The increased boundary pressure however reduces drawdown, and we observe that recovery relative to the gas in place R_{gIN} slows down, giving an opposite, but not contradicting trend with R_g.

Variation of _initial radius_ r_0 is illustrated in Fig. 10. The main impact is on intrinsic permeability which increases with radius and gives faster recovery. Also, at higher pore radii, slip effects are less significant and apparent permeability is almost constant at 15 μD for 60 nm, while it increases from 0.7 to 1 μDat low pressure for 12 nm, see Fig. 5. The relatively higher permeability at low pressures for low pore radii, is reflected in the spatial distributions of M_n where the low M_n (or low pressures) are less delayed than at high pore radius, compared to the fastest traveling M_n (which equals 1). Consequently, lower recovery at t_c results for larger radii. Had the compressibility been high (30 times the reference), we see from Fig. 5 that intrinsic permeability would be reduced almost linearly with pressure towards half the original value. The apparent permeability would counteract this effect more at low
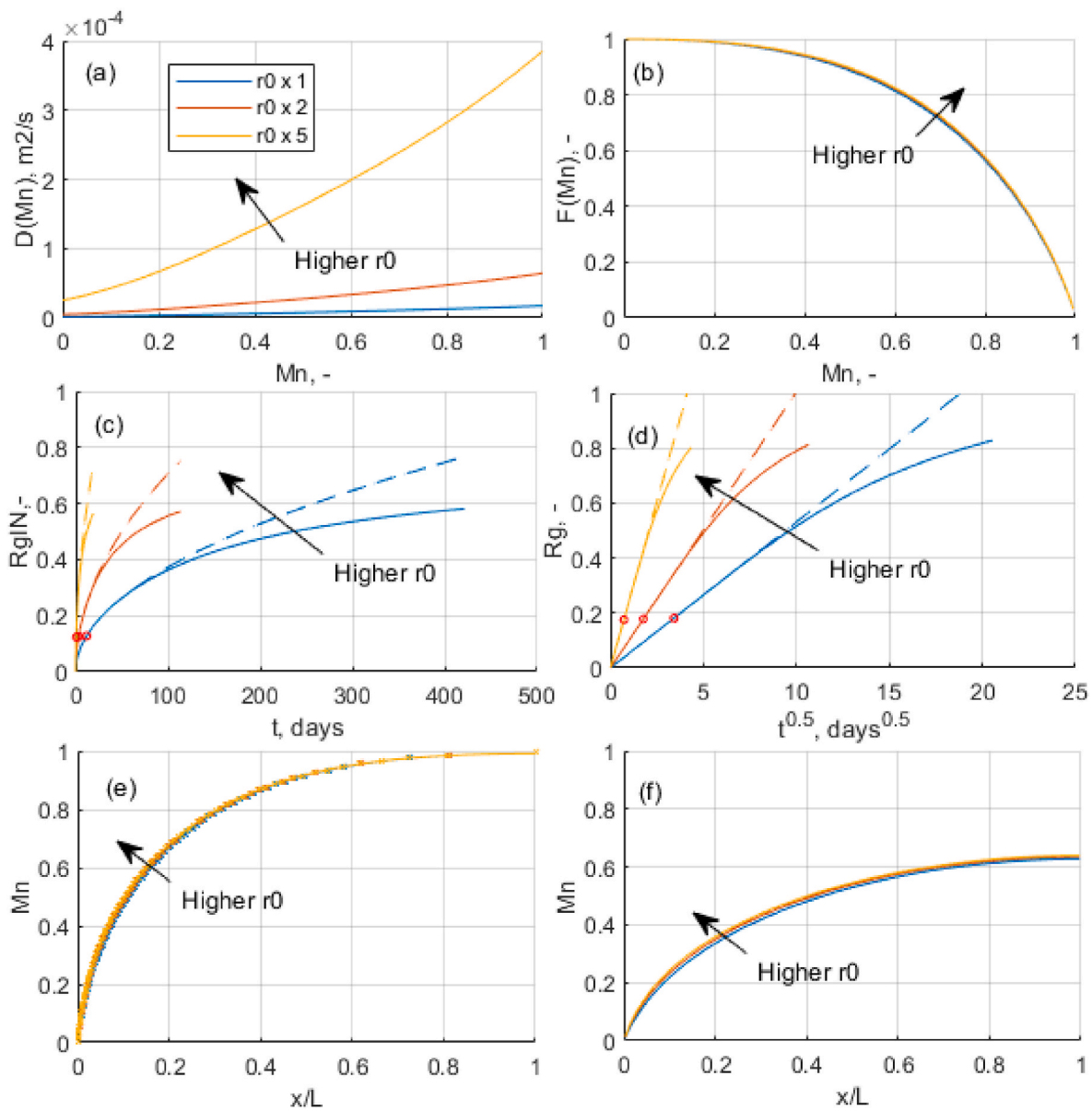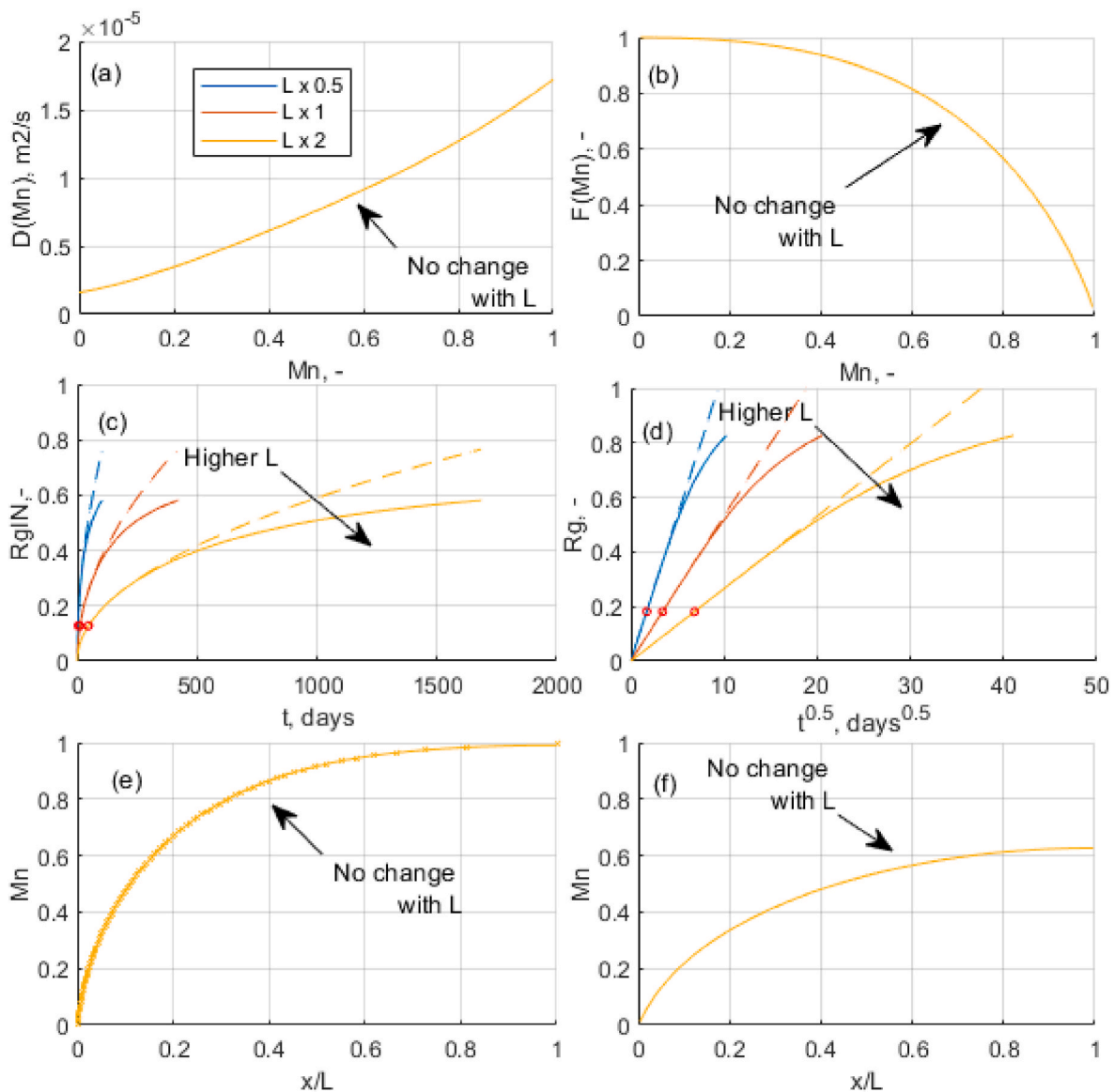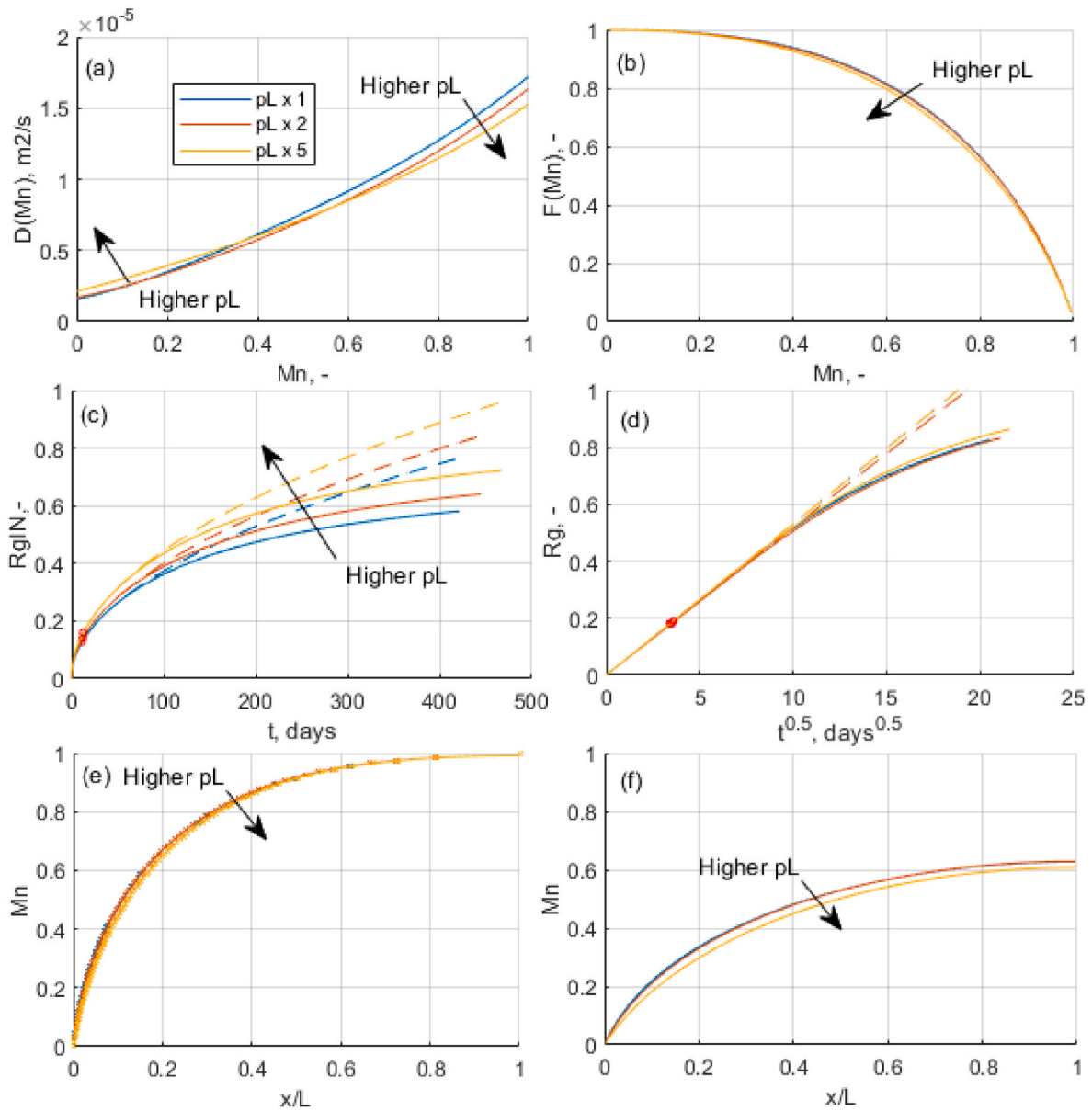
Fig. 12. The role of Langmuir pressure p_L (in factors times the reference value) on (a) $D(M)$, (b) $F(M)$, (c) recovery R_{gIN} vs time, (d) normalized recovery R_g vs square root of time, spatial profiles of M_n at (e) $t = t_c$ and (f) $t = 9t_c$. In the recovery plots dashed lines indicate the semi-analytical solution and the red circle the point where it ceases to be valid. In the spatial plot at $t = t_c$, crosses indicate the semi-analytical solution.

radius. Increased compressibility would thus delay propagation of low pressures more than high pressures, but the relative impact would be less for low radii.

System length L was varied in Fig. 11. This parameter does not appear in the calculation of A, F or D, and the functions $D(M), F(M)$ are therefore not changing. The time scales τ, t_c however both increase with L^2, see (16) and (17), and higher length is therefore seen to increase recovery time. The spatial profiles at equal scaled times are equal.

In Fig. 12 the _Langmuir pressure_ p_L was varied. Higher p_L gives more similar amount of desorption per pressure change than at low p_L where little desorption occurs at high pressures. The contribution from adsorption in $\frac{dM}{dp}$ (which is $\rho_b \frac{da}{dp}$) becomes more constant for high p_L instead of high at low pressure and low at high pressure. This results in a flatter $D(M)$, where D is lowered at high pressure and increased at low pressure. This trend makes low pressures less delayed than higher pressures and higher recovery at t_c. The overall magnitude of $D(M)$ does not appear to change and very similar recovery curves R_g result,

meaning it takes similar time to recover similar fractions of the producible gas. However, the initial gas in place and end recovery are both affected by p_L giving recovery curves R_{gIN} that differ more significantly. The increased flatness of the D function with higher p_L can be related to a higher $|D|_{0.5}$ and similar to Fig. 2b and **c** we see that the F function is reduced and the spatial profiles $M\left(\frac{x}{L}\right)$ at t_c are reduced, consistent with a slightly higher recovery R_g at the critical time.

3.5. Scaling of recovery

A variety of parameter combinations, as listed in Table 3 were run to generate 17 different recovery curves as shown in Fig. 13a. From the table, we see that 6 parameters are varied, 5 of which are nonlinearly related to the performance and in half the cases 2 or more parameters are varied from the reference values simultaneously. Each case was run until $t = 36t_c$. The resulting curves demonstrate a great span in recovery levels (R_{gIN} from 25 to 70%) and time scales (20–800 d). All the cases

Table 3
Parameter combinations for cases used in scaling example. The values indicate the factor each parameter is multiplied by compared to the reference values. Differences from the reference case are highlighted with bold.

Case ID	Compressi-bility	Adsorption capacity	Boundary pressur	Initial poreradius	Length	Langmuir pressure
	c_r	a_{max}	p_b	r_0	L	p_L
1	1	1	1	1	1	1
2	**30**	1	1	1	1	1
3	1	**0.35**	1	1	1	1
4	1	**5**	1	1	1	1
5	1	1	**3**	1	1	1
6	1	1	1	**5**	1	1
7	1	1	1	1	**0.5**	1
8	1	1	1	1	1	**2**
9	1	1	1	1	1	**5**
10	**30**	**0.35**	1	1	1	1
11	**30**	**5**	1	1	1	1
12	**30**	**0.35**	**3**	1	**0.5**	1
13	**30**	**5**	**3**	1	**0.5**	1
14	**30**	**0.35**	1	**5**	1	1
15	**30**	**5**	1	**5**	1	1
16	**30**	**0.35**	**3**	**5**	**2**	**5**
17	**30**	**5**	**3**	**5**	**2**	**5**

were scaled by presenting R_g against $\sqrt{\frac{t}{\tau}}$ in Fig. 13b. It is seen that all the curves fall on the same line at early times and do not differ significantly until R_g reaches between 0.35 and 0.5. Also, at late times the curves are closely collected as a consequence of the scaling, but can be seen to differ. The scaled curves were colored according to their value of $|D|_{0.5}$. It is seen that the curves can be grouped well by this parameter and that at late times a curve with high $|D|_{0.5}$ can be expected to have higher recovery R_g than a curve with low $|D|_{0.5}$. The recovery at the critical time, the highest value when the semi-analytical solution is valid, is plotted against $|D|_{0.5}$ in Fig. 13c. The range of $|D|_{0.5}$ is between 0.1 and 0.4, which is consistent with that the functions $D(M_n)$ are increasing, as also seen in the previous examples. The recovery at critical time increases close to linearly with $|D|_{0.5}$ from ~0.12 to ~0.22. The deviation from the semi-analytical solution (the square root of scaled time line) is noticeable at 0.2–0.25 recovery units higher.

3.6. Proposed new effective diffusion coefficient

We have shown that regardless the form of $D(M)$, recovery follows a square root of time profile before encountering the no-flow boundary. There hence exists a constant characteristic D_{ch} which gives the exact same root of time profile at early times, as represented by the resulting flux coefficient A:

$$A(D(M)) = A(D_{ch}) \tag{82}$$

The late time behavior and onset of late time may differ by the constant vs nonconstant shape of D. The specific value D_{ch} depends on the system parameters, but we assume it can be approximated by selecting a representative value of D systematically. The 17 cases listed in Table 3 were run to evaluate A_{true} (where the full nonlinear diffusion coefficient was applied) and A_{ch} (based on a constant D_{ch}). The following approaches to estimate D_{ch} were tested:

- D_{ch}^{m-ar}: the arithmetic mean of $D(M)$,
- D_{ch}^{m-h}: the harmonic mean of $D(M)$,
- D_{ch}^{M-av}: evaluation of D at $M_{av} = 0.5(M_b + M_0)$,
- D_{ch}^{*}: evaluate $\rho \frac{k_a}{\mu}$ at the average pressure and $\frac{dM}{dp} \approx \frac{\Delta M}{\Delta p}$ based on end pressures.
- $D_{ch}^{m-ar,corr}$: the arithmetic mean of $D(M)$ multiplied by the correction factor $\frac{A}{A_{conD}}$ as function of $|D|_{0.5}$, taken from (77).

Mathematically these relations are expressed as:

$$D_{ch}^{m-ar} = \frac{1}{M_0 - M_b} \int_{M_b}^{M_0} D(M)dM = \frac{1}{M_0 - M_b} \int_{M_b}^{M_0} \rho \frac{k_a}{\mu} \frac{dp}{dM} dM, \tag{83}$$

$$D_{ch}^{m-h} = \frac{1}{M_0 - M_b} \left[\int_{M_b}^{M_0} \frac{dM}{D(M)} \right]^{-1} = \frac{1}{M_0 - M_b} \left[\int_{M_b}^{M_0} \left(\rho \frac{k_a}{\mu} \frac{dp}{dM} \right)^{-1} dM \right]^{-1}, \tag{84}$$

$$D_{ch}^{M-av} = D(M_{av}), \tag{85}$$

$$D_{ch}^{*} = \left[\rho \frac{k_a}{\mu} \right]_{p_{av}} \bigg/ \left(\frac{\Delta M}{\Delta p} \right), \left(\frac{\Delta M}{\Delta p} \right) = \frac{[\varphi\rho + \rho_b a]_{p_0} - [\varphi\rho + \rho_b a]_{p_b}}{p_0 - p_b} \tag{86}$$

$$M_{av} = 0.5(M_0 + M_b) = 0.5\left([\varphi\rho + \rho_b a]_{p0} + [\varphi\rho + \rho_b a]_{pb}\right) \tag{87}$$

$$p_{av} = 0.5(p_0 + p_b) \tag{88}$$

$$D_{ch}^{m-ar,corr} = D_{ch}^{m-ar} \cdot \left[\frac{A}{A_{conD}} \right] \left(|D|_{0.5} \right) \tag{89}$$

The arithmetic mean (83) was suggested to scale nonlinear capillary diffusion coefficients for COUSI in Andersen et al. (2014). The use of a harmonic mean (84) better reflects the presence of small values. Evaluation of D at a characteristic input (85) has been applied for scaling COUSI by Zhou et al. (2002) and Standnes and Andersen (2017). Berawala et al. (2019) and Berawala and Andersen (2020) scaled shale gas production with pressure depletion in a fracture-matrix system accounting for different mechanisms using a similar form as (86) where the flux coefficient was evaluated at the mean pressure and the impact of adsorption and rock compressibility included by a retardation factor, $R = \frac{\Delta M}{\Delta p}$ (converted to the current notation).

The calculated flux coefficient values of A_{true} and the 5 different estimates of $A(D_{ch})$ are listed in Table 4 for all 17 cases together with the values of $|D|_{0.5}$ and resulting correction factor $\left[\frac{A}{A_{conD}} \right] \left(|D|_{0.5} \right)$ calculated from (77). The 5 estimates are plotted against A_{true} in Fig. 14 together with best-fit linear relations and the coefficients of determination R^2. For all estimates there is obtained a very strong correlation, with the lowest $R^2 = 0.9853$ when harmonic mean is used. The second highest $R^2 = 0.9987$ is obtained when the coefficient is evaluated at M_{av} which is thus a relatively simple and fast estimation. The best estimate is obtained when using the arithmetic mean with correction factor, with $R^2 = 0.9999$. Note that the correction factor was predicted in these examples
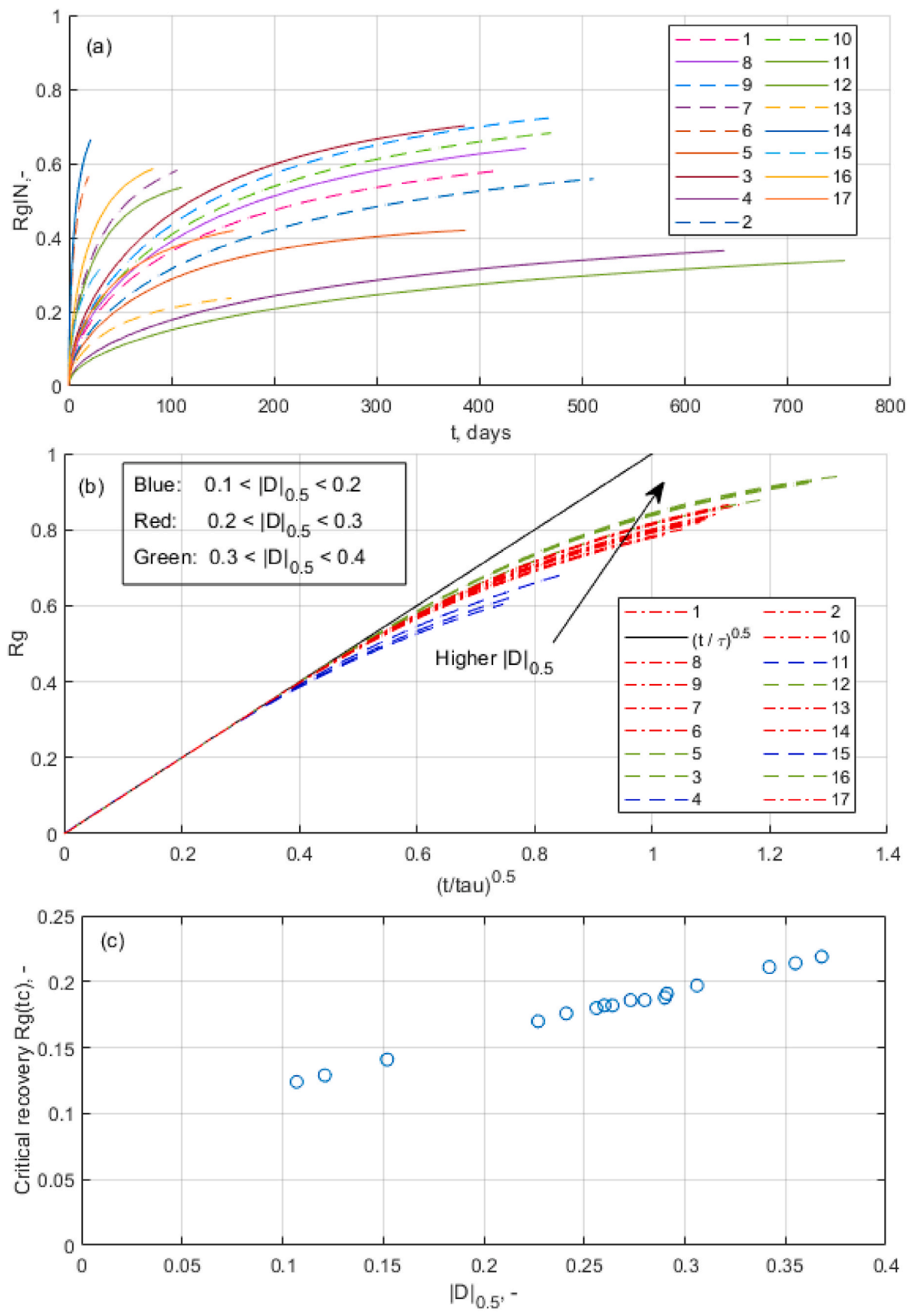
Fig. 13. Recovery R_{gIN} vs time (a) for a varied parameter dataset. R_g vs square root of scaled time (b) to where each case is colored according to the value of $|D|_{0.5}$. In (c) the recovery at the critical time is plotted against $|D|_{0.5}$ for each case.

Table 4
Calculated values of flux coefficients for the cases in Table 3.

Case ID	A_{true}	$A(D_{ch}^{m-ar})$	$A(D_{ch}^{m-h})$	$A(D_{ch}^{M-av})$	$A(D_{ch}^{*})$	$|D|_{0.5}$	Corr fac $\left(\frac{A}{A_{conD}}\right)$	$A(D_{ch}^{m-ar})$ ·corr fac
1	0.0194	0.0229	0.0186	0.0222	0.0238	0.260	0.838	0.0192
2	0.0166	0.0203	0.0152	0.0192	0.0204	0.227	0.813	0.0165
3	0.0184	0.0210	0.0184	0.0206	0.0218	0.306	0.873	0.0183
4	0.0243	0.0324	0.0206	0.0266	0.0336	0.152	0.751	0.0243
5	0.0151	0.0168	0.0160	0.0166	0.0171	0.368	0.916	0.0154
6	0.0883	0.1065	0.0815	0.1026	0.1111	0.241	0.824	0.0877
7	0.0194	0.0229	0.0186	0.0222	0.0238	0.260	0.838	0.0192
8	0.0200	0.0236	0.0194	0.0226	0.0244	0.264	0.841	0.0199
9	0.0204	0.0236	0.0204	0.0228	0.0244	0.291	0.862	0.0203
10	0.0159	0.0186	0.0155	0.0180	0.0187	0.273	0.848	0.0158
11	0.0205	0.0286	0.0160	0.0219	0.0288	0.121	0.724	0.0207
12	0.0135	0.0148	0.0139	0.0145	0.0148	0.355	0.907	0.0134
13	0.0166	0.0193	0.0167	0.0182	0.0194	0.280	0.853	0.0165
14	0.0729	0.0867	0.0686	0.0838	0.0874	0.256	0.835	0.0724
15	0.0936	0.1333	0.0679	0.0993	0.1343	0.107	0.712	0.0949
16	0.0642	0.0708	0.0661	0.0694	0.0711	0.342	0.898	0.0636
17	0.0921	0.1062	0.0931	0.1004	0.1066	0.290	0.861	0.0914

and the good performance supports its applicability.

The true flux coefficient A_{true} strongly correlates with the estimated ones. Looking at the linear trends we do however see signs of either systematic underestimation (on average 8.6% lower estimated flux using D_{ch}^{m-h}) or overestimation (on average $\sim 25\%$ higher estimated flux using D_{ch}^{*} and less overestimation for the remaining alternatives. For $D_{ch}^{m-ar,corr}$ the difference is negligible with less than 0.3% underestimation. The other misestimations can be corrected as follows:

$$D_1^{cor} = \frac{1}{1.231} D_{ch}^{m-ar}, \, D_2^{cor} = \frac{1}{0.914} D_{ch}^{m-h}, \tag{90}$$

$$D_3^{cor} = \frac{1}{1.108} D_{ch}^{M-av}, \, D_4^{cor} = \frac{1}{1.250} D_{ch}^{*}. \tag{91}$$

This follows since the flux is directly proportional to the diffusion coefficient, see (20) in the **Appendix**.

4. Discussion

We have demonstrated that shale gas production from matrix into a constant pressure boundary can be modeled as a nonlinear diffusion process which can be solved semi-analytically to yield self-similar behavior at early time and square root of recovery profiles. Although the solution has been shown to account for very many mechanisms, one should be aware that other flow mechanisms also may be relevant during shale gas production that the solution is not valid for. For instance, water from hydraulic fracturing or formation water may result in multiphase flow and water blockage phenomena reducing the effective gas permeability. Unpropped or poorly propped fractures can be sensitive to pressure depletion and lose conductivity as closure stress increases (Cipolla et al., 2010). Complex or dynamic (closing) fracture geometries and flow properties can restrict flow and give a pressure gradient rather than a constant pressure in the fracture (fracture-dominated flow). If the pressure in the fracture changes with time, the matrix conditions derived to model matrix flow are not valid.

If water blockage is negligible and the fractures have good conductivity, the semi-analytical solution can predict decline curves for shale gas. The decline curve is stated as one of the best techniques to estimate tight gas reserves (Holditch, 2006). It then follows that production rates should fall by the square root of time, at least for an early production phase. When the rate profile deviates from such a trend, the no-flow boundary has been met (likely some time ago) and it is possible to estimate gas in place. We have observed that deviation from the infinite-acting square root of time behavior takes place after 35–50% obtainable recovery indicating that it may be necessary to produce for a while before an accurate estimate is obtained.

Compared with counter-current spontaneous imbibition (COUSI) processes, which can be modeled with similar type equations, the nonlinear diffusion coefficient for shale gas production is nonzero and increasing with the mass variable, while for COUSI it is tied to zero at both end points. Our results show that the critical time and late time behavior are strongly determined by the parameter $|D|_{0.5}$, which could be explored also in such a context. The increase in D with pressure (or M) is related to the proportionality with gas density, which increases strongly with pressure. This increase also gives high pressures faster velocities than low pressures and results in a fairly low recovery when the no-flow boundary is encountered. The semi-analytical solution is however a good approximation long after this event, typically 0.2 to 0.25 recovery units higher.

5. Conclusions

In this work we have demonstrated that shale gas production from a 1D linear system can be modeled as a nonlinear diffusion process, even when accounting for shale and gas compressibility, apparent permeability and nonlinear adsorption. The main variable is then a bulk gas density M accounting for free gas, porosity and adsorbed gas. The ultimate behavior of the system is controlled by a nonlinear diffusion coefficient which is function of the bulk gas density. The impact of all system parameters can be described by how they impact this diffusion coefficient function. The behavior of the nonlinear diffusion equation was first investigated for arbitrarily shaped input diffusion coefficient functions $D(M)$ with same magnitude.

- Gas recovery follows exactly a square root of time profile until the critical time, defined by when the fastest pressure reaches the no-flow boundary.
- Recovery can be scaled such that all curves are identical at early time (before critical time). Then obtainable recovery equals the square root of scaled time.
- At late time, recovery is slower than by the square root of time.
- The fraction of the diffusion coefficient's area on the lower M interval, termed $0 < |D|_{0.5} < 1$, characterizes how skewed (non-flat) the D-function is and was found to be a very useful parameter to characterize recovery at the critical time and recovery at late time.
- The flux coefficient A stating how fast the square root of recovery occurs, could be predicted accurately based on the arithmetic mean of the diffusion coefficient and the parameter $|D|_{0.5}$. Diffusion coefficients with higher $|D|_{0.5}$ have higher flux.
- Functions with higher $|D|_{0.5}$ have higher recovery at the critical time (0.1–0.65 of obtainable recovery for $|D|_{0.5} \sim 0.1$ and ~ 0.9, respectively).
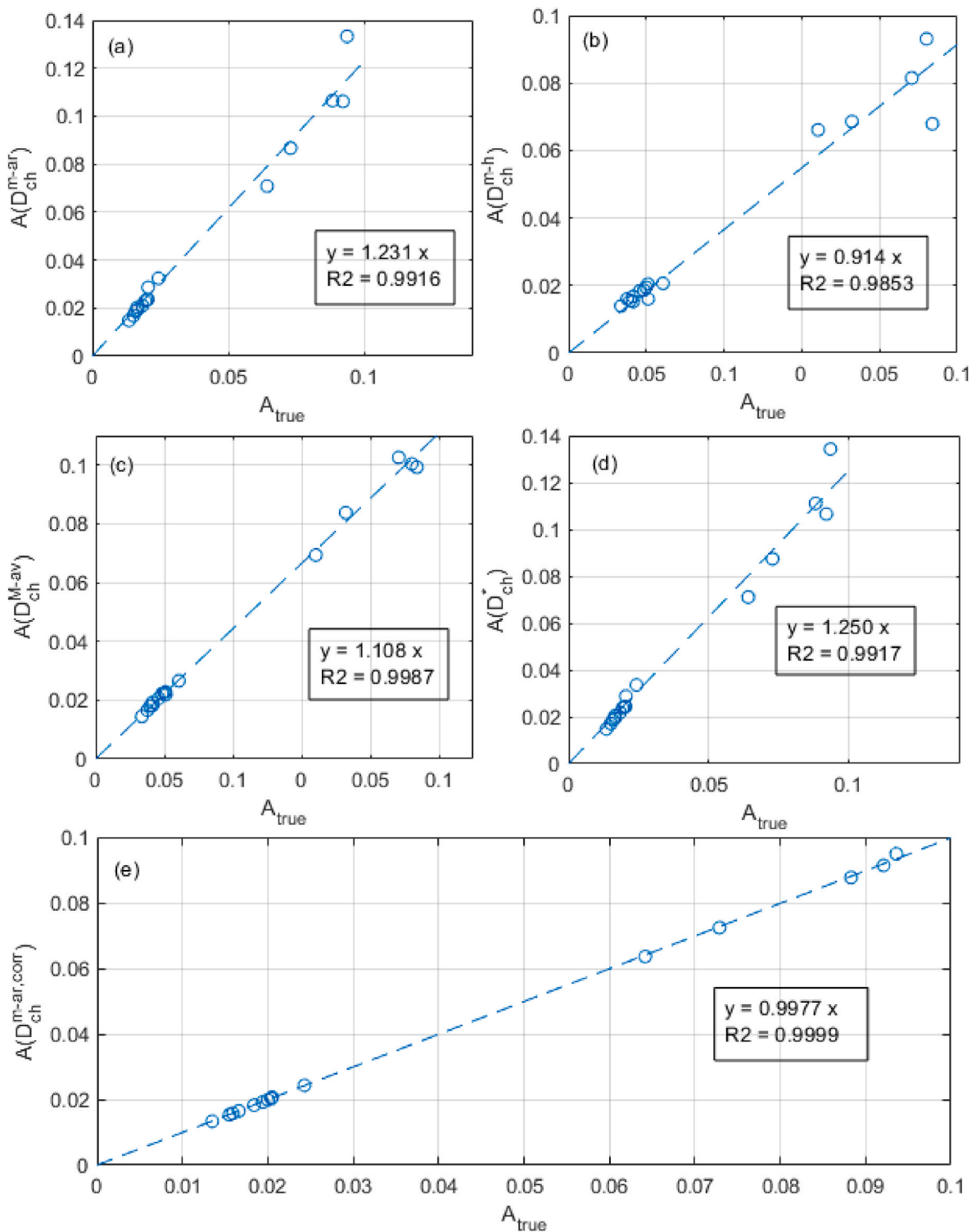
Fig. 14. Comparison of flux coefficients *A* based on different constant diffusion coefficients.

- The semi-analytical solution is a very good approximation to the true solution (evaluated numerically) also at late times, for recovery values typically 0.2–0.3 units higher than the recovery at the critical time.

The following conclusions were made when investigating systems with shale gas specific parameters:

- Most of the diffusion coefficients calculated for relevant shale gas systems were increasing with *M*, resulting in values of $|D|_{0.5}$ between 0.1 and 0.4. This is highly related to the proportionality with gas density, which increases strongly with pressure. As a result, obtainable recovery at the critical time was usually low, around 0.12 to 0.22. The semi-analytical square root of time solution was still a good approximation until obtainable recovery of 0.30–0.50, respectively.
- Each pressure (or *M*) travels at a speed that decreases by the square root of time and depends on *M*. By the diffusion process nature,

higher pressures travel at higher velocities. However, changes in input parameters that increase the diffusion coefficient more at low pressures than high, can reduce the separation between the high and low pressures.

- Higher well pressure (lower drawdown) increases the lower pressure limit and the average diffusion coefficient. This results in a faster rate of obtainable recovery with time, although the rate of recovery of gas initially in place is reduced.
- If permeability reduces significantly with pressure and adsorbed gas makes a high fraction of what is produced, it can be expected that $|D|_{0.5}$ is low which implies that a limited part of the recovery follows a square root time profile.

Appendix. Discretization

Consider the system:

$$\partial_t M = \partial_x(D(M)\partial_x M), D(M) = \rho \frac{k_a}{\mu} \frac{dp}{dM} \tag{92}$$

$$M(x, t=0) = M_0, M(x=0, t) = M_b, \partial_x M|_{x=L} = 0. \tag{93}$$

The system is discretized implicitly and the boundary conditions are implemented directly in the fluxes of the first and last cell:

$$\frac{M_i^{n+1} - M_i^n}{\Delta t} = \frac{1}{\Delta x^2} \left[D_{i+\frac{1}{2}}^{n+1}\left(M_{i+1}^{n+1} - M_i^{n+1}\right) - D_{i-\frac{1}{2}}^{n+1}\left(M_i^{n+1} - M_b\right) \right], (i=1) \tag{94}$$

$$\frac{M_i^{n+1} - M_i^n}{\Delta t} = \frac{1}{\Delta x^2} \left[D_{i+\frac{1}{2}}^{n+1}\left(M_{i+1}^{n+1} - M_i^{n+1}\right) - D_{i-\frac{1}{2}}^{n+1}\left(M_i^{n+1} - M_{i-1}^{n+1}\right) \right], (i=2:N-1) \tag{95}$$

$$\frac{M_i^{n+1} - M_i^n}{\Delta t} = \frac{1}{\Delta x^2} \left[0 - D_{i-\frac{1}{2}}^{n+1}\left(M_i^{n+1} - M_{i-1}^{n+1}\right) \right], (i=N) \tag{96}$$

where the coefficients are evaluated as:

$$D_{i-\frac{1}{2}}^{n+1} = 2D\left(M_i^{n+1}\right), (i=1) \tag{97}$$

$$D_{i-\frac{1}{2}}^{n+1} = \frac{1}{2}\left[D\left(M_{i-1}^{n+1}\right) + D\left(M_i^{n+1}\right)\right], (i=2:N) \tag{98}$$

The factor 2 in (97) is included to evaluate the gradient between the center of cell 1 and its left boundary instead of between the centers of two cells. Introducing the notation $\gamma = \frac{\Delta t}{\Delta x^2}$ and rearranging, this system can be written as:

$$\left(1 + \gamma D_{i+\frac{1}{2}}^{n+1} + \gamma D_{i-\frac{1}{2}}^{n+1}\right) M_i^{n+1} - \gamma D_{i+\frac{1}{2}}^{n+1} M_{i+1}^{n+1} = M_i^n + \gamma D_{i-\frac{1}{2}}^{n+1} M_b, (i=1) \tag{99}$$

$$-\gamma D_{i-\frac{1}{2}}^{n+1} M_{i-1}^{n+1} + \left(1 + \gamma D_{i+\frac{1}{2}}^{n+1} + \gamma D_{i-\frac{1}{2}}^{n+1}\right) M_i^{n+1} - \gamma D_{i+\frac{1}{2}}^{n+1} M_{i+1}^{n+1} = M_i^n, (i=2:N-1) \tag{100}$$

$$-\gamma D_{i-\frac{1}{2}}^{n+1} M_{i-1}^{n+1} + \left(1 + \gamma D_{i-\frac{1}{2}}^{n+1}\right) M_i^{n+1} = M_i^n, (i=N) \tag{101}$$

This corresponds to the following tridiagonal linear system of equations:

$$
\begin{bmatrix}
d_1 & e_1 & & & & & & \\
c_2 & d_2 & e_2 & & & & & \\
 & c_3 & d_3 & e_3 & & & & \\
 & & & & & & & \\
 & & & c_i & d_i & e_i & & \\
 & & & & c_{i+1} & d_{i+1} & e_{i+1} & \\
 & & & & & & & \\
 & & & & & c_{N-1} & d_{N-1} & e_{N-1} \\
 & & & & & & c_N & d_N
\end{bmatrix}
\begin{bmatrix}
M_1 \\ M_2 \\ \\ M_{i-1} \\ M_i \\ M_{i+1} \\ \\ M_{N-1} \\ M_N
\end{bmatrix}
=
\begin{bmatrix}
b_1 \\ b_2 \\ \\ b_{i-1} \\ b_i \\ b_{i+1} \\ \\ b_{N-1} \\ b_N
\end{bmatrix}
\tag{102}
$$

with the following definitions:

$$
b_i = M_i^n + \gamma D_{i-\frac{1}{2}}^{n+1} M_b, d_i = \left(1 + \gamma D_{i+\frac{1}{2}}^{n+1} + \gamma D_{i-\frac{1}{2}}^{n+1}\right), e_i = -\gamma D_{i+\frac{1}{2}}^{n+1}, (i=1)
\tag{103}
$$

$$
b_i = M_i^n, c_i = -\gamma D_{i-\frac{1}{2}}^{n+1}, d_i = \left(1 + \gamma D_{i+\frac{1}{2}}^{n+1} + \gamma D_{i-\frac{1}{2}}^{n+1}\right), e_i = -\gamma D_{i+\frac{1}{2}}^{n+1}, (i=2:N-1)
\tag{104}
$$

$$
b_i = M_i^n, c_i = -\gamma D_{i-\frac{1}{2}}^{n+1}, d_i = \left(1 + \gamma D_{i-\frac{1}{2}}^{n+1}\right), (i=N)
\tag{105}
$$

The terms b_i, c_i, d_i, e_i depending on M_i^{n+1} are considered constants such that the system can be solved as linear equations. After time step n they are first estimated using the solution M_i^n. Solving the system gives improved estimates for M_i^{n+1} and the terms, which after enough iterations gives the same estimate M_i^{n+1}.

The linear system is solved directly using the Thomas algorithm: First define the sequence of parameters $\alpha_i, S_i (i=1:N)$

$$
\alpha_1 = d_1, S_1 = b_1,
\tag{106}
$$

$$
\alpha_i = d_i - \frac{c_i e_{i-1}}{\alpha_{i-1}}, S_i = b_i - \frac{c_i S_{i-1}}{\alpha_{i-1}}, (i=2:N)
\tag{107}
$$

Then calculate M_i as:

$$
M_N = \frac{S_N}{\alpha_N}, M_i = \frac{S_i - e_i M_{i+1}}{\alpha_i}, (i=N-1:1)
\tag{108}
$$

At a given time step the numerical solution was evaluated to converge if the estimated solution vectors from last M_{est} and current iteration M_{est}^{new} were sufficiently equal: $\frac{|M_{est} - M_{est}^{new}|}{N_x^{0.5}} < 10^{-9}$ kg/m3.

References

Abd, A.S., Elhafyan, E., Siddiqui, A.R., Alnoush, W., Blunt, M.J., Alyafei, N., 2019. A review of the phenomenon of counter-current spontaneous imbibition: analysis and data interpretation. J. Petrol. Sci. Eng. 180, 456–470.

Andersen, P.Ø., Evje, S., Kleppe, H., 2014. A model for spontaneous imbibition as a mechanism for oil recovery in fractured reservoirs. Transport Porous Media 101 (2), 299–331.

Andersen, P.Ø., Qiao, Y., Standnes, D.C., Evje, S., 2019a. Cocurrent spontaneous imbibition in porous media with the dynamics of viscous coupling and capillary backpressure. SPE J. 24, 158–177, 01.

Andersen, P.Ø., Brattekås, B., Nødland, O., Lohne, A., Føyen, T.L., Fernø, M.A., 2019b. Darcy-Scale simulation of Boundary-Condition effects during Capillary-Dominated flow in high-permeability systems. SPE Reservoir Eval. Eng. 22, 673–691, 02.

Andersen, P.Ø., Nesvik, E.K., Standnes, D.C., 2020. Analytical solutions for forced and spontaneous imbibition accounting for viscous coupling. J. Petrol. Sci. Eng. 186, 106717.

Berawala, D.S., Andersen, P.Ø., Ursin, J.R., 2019. Controlling parameters during continuum flow in shale-gas production: a fracture/matrix-modeling approach. SPE J. 24, 1–378, 03.

Berawala, D.S., Andersen, P.Ø., 2020. Numerical investigation of Non-Darcy flow regime transitions in shale gas production. J. Petrol. Sci. Eng. 190, 107114.

Cao, C., Lv, Z., Li, L., Du, L., 2016. Geochemical characteristics and implications of shale gas from the longmaxi formation, sichuan basin, China. J. Nat. Gas. Geosci. 1 (2), 131–138.

Chen, K.P., Shen, D., 2018. Mechanism of fluid production from the nanopores of shale. Mech. Res. Commun. 88, 34–39.

Cheng, Y., 2012. Impact of water dynamics in fractures on the performance of hydraulically fractured wells in gas-shale reservoirs. J. Can. Petrol. Technol. 51, 143–151, 02.

Cipolla, C.L., Lolon, E.P., Erdle, J.C., Rubin, B., 2010. Reservoir modeling in shale-gas reservoirs. SPE Reservoir Eval. Eng. 13, 638–653, 04.

Civan, F., Rai, C.S., Sondergeld, C.H., 2011. Shale-gas permeability and diffusivity inferred by improved formulation of relevant retention and transport mechanisms. Transport Porous Media 86 (3), 925–944.

Curtis, J.B., 2002. Fractured shale-gas systems. AAPG Bull. 86 (11), 1921–1938.

Darabi, H., Ettehad, A., Javadpour, F., Sepehrnoori, K., 2012. Gas flow in ultra-tight shale strata. J. Fluid Mech. 710, 641.

Darishchev, A., Lemouzy, P., Rouvroy, P., 2013. January). On simulation of flow in tight and shale gas reservoirs. In: SPE Unconventional Gas Conference and Exhibition. Society of Petroleum Engineers.

Dong, J.J., Hsu, J.Y., Wu, W.J., Shimamoto, T., Hung, J.H., Yeh, E.C., Sone, H., 2010. Stress-dependence of the permeability and porosity of sandstone and shale from TCDP Hole-A. Int. J. Rock Mech. Min. Sci. 47 (7), 1141–1157.

Florence, F.A., Rushing, J., Newsham, K.E., Blasingame, T.A., 2007. January). Improved permeability prediction relations for low permeability sands. In: Rocky Mountain Oil & Gas Technology Symposium. Society of Petroleum Engineers.

Heller, R., Zoback, M., 2014. Adsorption of methane and carbon dioxide on gas shale and pure mineral samples. J. Unconventional Oil Gas Res. 8, 14–24.

Heller, R., Vermylen, J., Zoback, M., 2014. Experimental investigation of matrix permeability of gas shales. AAPG Bull. 98 (5), 975–995.

Holditch, S.A., 1979. Factors affecting water blocking and gas flow from hydraulically fractured gas wells. J. Petrol. Technol. 31 (12), 1–515.

Holditch, S.A., 2006. Tight gas sands. J. Petrol. Technol. 58, 86–93, 06.

Javadpour, F., Fisher, D., Unsworth, M., 2007. Nanoscale gas flow in shale gas sediments. J. Can. Petrol. Technol. 46 (10).

Jiang, J., Yang, J., 2018. Coupled fluid flow and geomechanics modeling of stress-sensitive production behavior in fractured shale gas reservoirs. Int. J. Rock Mech. Min. Sci. 101, 1–12.

Jin, Y., Chen, K.P., 2019. Fundamental equations for primary fluid recovery from porous media. J. Fluid Mech. 860, 300–317.

Klewiah, I., Berawala, D.S., Walker, H.C.A., Andersen, P.Ø., Nadeau, P.H., 2020. Review of experimental sorption studies of CO2 and CH4 in shales. J. Nat. Gas Sci. Eng. 73, 103045.

Klinkenberg, L.J., 1941. January). The permeability of porous media to liquids and gases. In: Drilling and Production Practice. American Petroleum Institute.

Knudsen, M., 1909. Die Gesetze der Molekularströmung und der inneren Reibungsströmung der Gase durch Röhren. Ann. Phys. 333 (1), 75–130.

Kuuskraa, V.A., Sedwick, K., Yost, A.B., 1985. January). Technically recoverable Devonian shale gas in Ohio, West Virginia, and Kentucky. In: SPE Eastern Regional Meeting. Society of Petroleum Engineers.

Kuuskraa, V., Stevens, S.H., Moodhe, K.D., 2013. Technically Recoverable Shale Oil and Shale Gas Resources: an Assessment of 137 Shale Formations in 41 Countries outside the United States. US Energy Information Administration, US Department of Energy.

Langmuir, I., 1918. The adsorption of gases on plane surfaces of glass, mica and platinum. J. Am. Chem. Soc. 40 (9), 1361–1403.

Lee, A.L., Gonzalez, M.H., Eakin, B.E., 1966. The viscosity of natural gases. J. Petrol. Technol. 18 (08), 997-1.

Loeb, L.B., 1934. Kinetic Theory. McGrow-Hill, New York, p. 132.

March, R., Doster, F., Geiger, S., 2016. Accurate early-time and late-time modeling of countercurrent spontaneous imbibition. Water Resour. Res. 52 (8), 6263–6276.

Mason, G., Morrow, N.R., 2013. Developments in spontaneous imbibition and possibilities for future work. J. Petrol. Sci. Eng. 110, 268–293.

McWhorter, D.B., Sunada, D.K., 1990. Exact integral solutions for two-phase flow. Water Resour. Res. 26 (3), 399–413.

Mengal, S.A., Wattenbarger, R.A., 2011. January). Accounting for adsorbed gas in shale gas reservoirs. SPE Middle East Oil and Gas Show and Conference. Society of Petroleum Engineers.

Mullen, J., 2010. January). Petrophysical characterization of the eagle ford shale in south Texas. In: Canadian Unconventional Resources and International Petroleum Conference. Society of Petroleum Engineers.

Nuttal, B.C., Eble, C., Bustin, R.M., Drahovzal, J.A., 2005. Analysis of Devonian black shales in Kentucky for potential carbon dioxide sequestration and enhanced natural gas production. In: Greenhouse Gas Control Technologies, vol. 7. Elsevier Science Ltd, pp. 2225–2228.

Pan, Z., Connell, L.D., 2015. Reservoir simulation of free and adsorbed gas production from shale. J. Nat. Gas Sci. Eng. 22, 359–370.

Patzek, T.W., 2017, October. Knudsen-like scaling may be inappropriate for gas shales. In: SPE Annual Technical Conference and Exhibition. OnePetro.

Peng, D.Y., Robinson, D.B., 1976. A new two-constant equation of state. Ind. Eng. Chem. Fundam. 15 (1), 59–64.

Qiao, Y., Andersen, P.Ø., Evje, S., Standnes, D.C., 2018. A mixture theory approach to model co-and counter-current two-phase flow in porous media accounting for viscous coupling. Adv. Water Resour. 112, 170–188.

Rubin, C., Zamirian, M., Takbiri-Borujeni, A., Gu, M., 2019. Investigation of gas slippage effect and matrix compaction effect on shale gas production evaluation and hydraulic fracturing design based on experiment and reservoir simulation. Fuel 241, 12–24.

Schmid, K.S., Geiger, S., Sorbie, K.S., 2011. Semianalytical solutions for cocurrent and countercurrent imbibition and dispersion of solutes in immiscible two-phase flow. Water Resour. Res. 47 (2).

Schmid, K.S., Geiger, S., 2012. Universal scaling of spontaneous imbibition for water-wet systems. Water Resour. Res. 48 (3).

Shi, J., Zhang, L., Li, Y., Yu, W., He, X., Liu, N., Wang, T., 2013. November). Diffusion and flow mechanisms of shale gas through matrix pores and gas production forecasting. In: SPE Unconventional Resources Conference Canada (OnePetro).

Standnes, D.C., Andersen, P.Ø., 2017. Analysis of the impact of fluid viscosities on the rate of countercurrent spontaneous imbibition. Energy Fuel. 31 (7), 6928–6940.

Sun, H., Chawathe, A., Hoteit, H., Shi, X., Li, L., 2015. Understanding shale gas flow behavior using numerical simulation. SPE J. 20, 142–154, 01.

Swami, V., Settari, A.T., Javadpour, F., 2013. June). A numerical model for multi-mechanism flow in shale gas reservoirs with application to laboratory scale testing. In: EAGE Annual Conference & Exhibition Incorporating SPE Europec (OnePetro).

Yu, W., Sepehrnoori, K., 2014. Simulation of gas desorption and geomechanics effects for unconventional gas reservoirs. Fuel 116, 455–464.

Zhou, D., Jia, L., Kamath, J., Kovscek, A.R., 2002. Scaling of counter-current imbibition processes in low-permeability porous media. J. Petrol. Sci. Eng. 33 (1–3), 61–74.

Glossary

Roman

A: Flux proportionality coefficient, $kg/m2/s0.5$
a: Adsorbed mass gas per mass rock, kg/kg
a_{max}: Maximum capacity adsorbed mass gas per mass rock, kg/kg
c_r: Rock compressibility, Pa-1
C_1, C_2: Integration constants
D: Nonlinear diffusion coefficient, m2/s
D_1, D_2: Curve parameters,
$|D|_{0.5}$: Area of diffusion coefficient between $M_n = 0$ and 0.5,
F: Flow function,
k_a: Apparent permeability, m^2
K_n: Knudsen number,
k_∞: Intrinsic permeability
L: System length, m
M: Bulk gas density, kg/m3
M_n: Normalized bulk gas density,
M_w: Molar weight, kg/mol
N: Total number grid blocks,
n: Curve exponent,
p: Gas pressure, Pa
p_L: Langmuir pressure, Pa
q: Mass flux, kg/m2/s
R: Universal gas constant, J/mol/K
R_g: Gas recovery,
r: Pore radius, m
r_{EP}: Ratio of end points in diffusion coefficient,
T: Absolute temperature, K
t: Time, s
u: Darcy velocity, m/s
x: Length from open side, m
z: Gas compressibility factor,

Greek

α_K: Rarefaction coefficient,
γ: Discretization parameter, m/s2
Δt: Time step, s
Δx: Grid length, m
λ: Mean free path length, m
τ_f: Formation tortuosity,
τ: Time scale of recovery, s
ρ_r: Rock density, kg/m3
μ: Gas viscosity, Pa s
ρ: Gas density, kg/m^3
φ: Porosity,

Indices

0: Initial
b: Boundary
g: Gas
i: Grid block index
n: Time step index

Abbreviations

COUSI: Counter-current spontaneous imbibition